The Astronomical Journal, 151:66 (20pp), 2016 March doi:10.3847/0004-6256/151/3/66
© 2016. The American Astronomical Society. All rights reserved.

DETERMINING THE AGE OF THE *KEPLER* OPEN CLUSTER NGC 6819 WITH A NEW TRIPLE SYSTEM AND OTHER ECLIPSING BINARY STARS*

Lauren N. Brewer[1], Eric L. Sandquist[1], Robert D. Mathieu[2,9], Katelyn Milliman[2,9], Aaron M. Geller[3,4,9], Mark W. Jeffries, Jr.[1], Jerome A. Orosz[1], Karsten Brogaard[5,6], Imants Platais[7], Hans Bruntt[5], Frank Grundahl[5], Dennis Stello[8], and Søren Frandsen[5]

[1] San Diego State University, Department of Astronomy, San Diego, CA 92182, USA; ezereve@gmail.com, esandquist@mail.sdsu.edu, jorosz@mail.sdsu.edu, mjeffries11@gmail.com
[2] University of Wisconsin-Madison, Department of Astronomy, Madison, WI 53706, USA; mathieu@astro.wisc.edu, milliman@astro.wisc.edu
[3] Center for Interdisciplinary Exploration and Research in Astrophysics (CIERA) and Northwestern University, Department of Physics and Astronomy, 2145 Sheridan Road, Evanston, IL 60208, USA; a-geller@northwestern.edu
[4] Department of Astronomy and Astrophysics, University of Chicago, 5640 S. Ellis Avenue, Chicago, IL 60637, USA
[5] Stellar Astrophysics Centre, Department of Physics and Astronomy, Aarhus University, Ny Munkegade 120, DK-8000 Aarhus C, Denmark; kfb@phys.au.dk, bruntt@gmail.com, fgj@phys.au.dk, srf@phys.au.dk
[6] Department of Physics & Astronomy, University of Victoria, P.O. Box 3055, Victoria, BC V8W 3P6, Canada
[7] Department of Physics and Astronomy, The Johns Hopkins University, Baltimore, MD 21218, USA; imants@pha.jhu.edu
[8] Sydney Institute for Astronomy (SIfA), School of Physics, University of Sydney, Sydney, NSW 2006, Australia; stello@physics.usyd.edu.au
Received 2015 October 14; accepted 2016 January 5; published 2016 February 18

ABSTRACT

As part of our study of the old (~2.5 Gyr) open cluster NGC 6819 in the *Kepler* field, we present photometric (*Kepler* and ground-based BVR_CI_C) and spectroscopic observations of the detached eclipsing binary WOCS 24009 (Auner 665; KIC 5023948) with a short orbital period of 3.6 days. WOCS 24009 is a triple-lined system, and we verify that the brightest star is physically orbiting the eclipsing binary using radial velocities and eclipse timing variations. The eclipsing binary components have masses $M_B = 1.090 \pm 0.010\,M_\odot$ and $M_C = 1.075 \pm 0.013\,M_\odot$, and radii $R_B = 1.099 \pm 0.006 \pm 0.005\,R_\odot$ and $R_C = 1.069 \pm 0.006 \pm 0.013\,R_\odot$. The bright non-eclipsing star resides at the cluster turnoff, and ultimately its mass will directly constrain the turnoff mass: our preliminary determination is $M_A = 1.251 \pm 0.057\,M_\odot$. A careful examination of the light curves indicates that the fainter star in the eclipsing binary undergoes a very brief period of total eclipse, which enables us to precisely decompose the light of the three stars and place them in the color–magnitude diagram (CMD). We also present improved analysis of two previously discussed detached eclipsing stars in NGC 6819 (WOCS 40007 and WOCS 23009) en route to a combined determination of the cluster's distance modulus $(m - M)_V = 12.38 \pm 0.04$. Because this paper significantly increases the number of measured stars in the cluster, we can better constrain the age of the CMD to be $2.21 \pm 0.10 \pm 0.20$ Gyr. Additionally, using all measured eclipsing binary star masses and radii, we constrain the age to $2.38 \pm 0.05 \pm 0.22$ Gyr. The quoted uncertainties are estimates of measurement and systematic uncertainties (due to model physics differences and metal content), respectively.

Key words: binaries: eclipsing – binaries: spectroscopic – open clusters and associations: individual (NGC 6819) – stars: evolution – techniques: photometric – techniques: spectroscopic

Supporting material: machine-readable tables

1. INTRODUCTION

Measurements of the masses and radii of the component stars in detached eclipsing binaries (DEB) can be used to precisely determine the age of the stars if at least one of the eclipsing stars has begun to evolve away from the main sequence. The use of mass and radius (*M–R*) measurements of eclipsing stars avoids or minimizes systematic uncertainties introduced by factors such as distance, interstellar reddening, and color–temperature conversions that can affect age measurements (Andersen 1991; Torres et al. 2010). When eclipsing binaries occur in star clusters, their utility increases dramatically because they place constraints on the age of *all* the stars in the cluster. Multiple DEBs in a cluster can provide *M–R* measurements for stars having a range in mass, and can constrain the age even more tightly. With a well-determined age for a cluster, the color–magnitude diagram (CMD) can be used to test the effects of evolution on an even larger number of stars. Comparisons of the masses and radii of eclipsing stars and the CMD with theoretical stellar models can also lead to deeper inferences about chemical composition variables such as helium abundance (Brogaard et al. 2011, 2012).

This study focuses on the rich open cluster NGC 6819, which has been observed thoroughly from the ground and with the *Kepler* spacecraft. NGC 6819 is a well-studied cluster: its CMD (Burkhead 1971; Lindoff 1972; Auner 1974; Rosvick & Vandenberg 1998; Kalirai et al. 2001; Yang et al. 2013) as well as stellar variability (Kaluzny & Shara 1988; Street et al. 2002, 2003, 2005; Talamantes et al. 2010) have been examined in multiple studies. In addition, the cluster has been part of the WIYN Open Cluster Survey (WOCS; Mathieu 2000) with comprehensive long-term radial-velocity (RV) studies presented by Hole et al. (2009) and Milliman et al. (2014).

Thanks to the nearly continuous monitoring and high precision photometry by *Kepler*, studies of stellar ages using

* This is paper 57 of the WIYN Open Cluster Study (WOCS).
[9] Visiting Astronomer, Kitt Peak National Observatory, National Optical Astronomy Observatories, which is operated by the Association of Universities for Research in Astronomy, Inc. (AURA) under cooperative agreement with the National Science Foundation.

multiple techniques have been kickstarted. Because several techniques can be applied within the same cluster, a comparison of results should ultimately improve our understanding of each. Basu et al. (2011) used asteroseismic data from *Kepler* to constrain basic properties of red giant stars and to place constraints on the cluster distance [$(m-M)_0 = 11.85 \pm 0.05$] and age (between 2.1 and 2.5 Gyr). Stellar rotation measurements have been used to examine the gyrochronological ages of two of the four open clusters in the *Kepler* field: NGC 6811 (Meibom et al. 2011) and NGC 6819 (Meibom et al. 2015). Kalirai et al. (2001) describes how the age of NGC 6819 can be found using the faint end of the white dwarf cooling sequence, and Bedin et al. (2015) present an age of 2.25 ± 0.20 Gyr using that technique. For our part, we have so far analyzed two eclipsing systems in NGC 6819 (WOCS 23009/KIC 5024447, Sandquist et al. 2013a; WOCS 40007/KIC 5113053, Jeffries et al. 2013).

In this paper we present the triple-lined system WOCS 24009 (also known as KIC 5023948/Auner 665; $\alpha_{2000} = 19^{\rm h}40^{\rm m}57\overset{\prime\prime}{.}82$, $\delta_{2000} = +40°09'27\overset{\prime\prime}{.}4$) to add to the grid of cluster stars with precisely determined masses and to further constrain the age of NGC 6819. We identify the three stars as follows: component A is the brightest contributor to spectra and is on a wide orbit around the short-period detached eclipsing binary made up of components B and C, where B is slightly brighter and more massive than C and is the star being eclipsed during primary eclipse, as we will discuss in the analysis sections. This system is promising because all three stars are bright enough to be studied spectroscopically, the three can be shown to be physically associated, and it contains one of the most evolved stars in the cluster whose mass can be directly determined from RV measurements.

In Section 2, we describe the observations we employed, and describe the improved spectroscopic analysis techniques that allowed us to minimize the mass and radius measurement uncertainties in the the face of three sets of blended lines. We also used these techniques to improve our previously presented measurements of WOCS 23009 and WOCS 40007. In Section 3, we discuss the membership of the system, and describe the modeling of the eclipsing binary and the orbit of the bright non-eclipsing star. In Section 4, we discuss the photometry of the stars, and use all three eclipsing systems in a combined analysis to derive the cluster distance modulus and age.

2. OBSERVATIONS AND DATA REDUCTION

Our datasets include ground-based and space-based *Kepler* photometric observations along with long-term RV observations. In addition to the work on the WOCS 24009 system, we also discuss improvements to the dataset for WOCS 40007 (Jeffries et al. 2013) below.

2.1. Ground-based Photometry

We obtained images in B, V, R_c, and I_c filters using the Mount Laguna Observatory (MLO) 1 m telescope. WOCS 24009 eclipse light curves were computed from two nights in 2010 in addition to dedicated nights in 2011, 2012, and 2014. The observations on nights of eclipses are given in Table 1. The dataset also includes earlier images presented by Talamantes et al. (2010). Exposure times were typically 300 or 600 s for B and V, 420 s for R_c, and 300 s for I_c. The CCD 2005 camera covers $13\overset{\prime}{.}7 \times 13\overset{\prime}{.}7$ on sky with a scale of $0\overset{\prime\prime}{.}41$ per pixel.

Table 1
Observed Nights at the Mount Laguna Observatory 1-m Telescope

Date	Filter	mJD Start[a]	$t_{\rm exp}$ (s)	N
2008 Jun 15	B	4633.699	180	22
2009 Jun 12	V	4994.701	120	147
2009 Oct 22	V	5126.589	120	59
2010 Jun 22	B	5370.708	600	34
2010 Sep 14	B, R_c	5454.781	600	7, 7
2011 May 22	B, V	5704.802	600, 600	6, 9
2011 Jun 02	B, V	5715.738	600, 600	9, 12
2011 Jun 11	V	5724.725	600	35
2011 Jul 03[b]	I_c	5746.677	300	41
2011 Jul 14	R_c	5757.660	420	62
2011 Jul 23[c]	I_c	5766.657	300	83
2011 Jul 25[b,c]	B, I_c	5768.662	300, 300	33, 41
2011 Aug 14	R_c	5788.639	420	65
2011 Aug 25	B, V	5799.627	600, 600	13, 21
2011 Sep 16	B, V	5821.631	600, 600	17, 15
2011 Oct 17	B, V	5852.582	300, 300	28, 20
2011 Oct 28	I_c	5863.587	300	44
2011 Nov 28	V	5894.557	300	34
2012 Apr 18	V, I_c	6036.838	300	18, 20
2014 Jun 8	B, V	6817.709	300, 300	45, 16
2014 Jul 20	B	6859.669	600	42

Notes.
[a] mJD = BJD—2 450 000.
[b] Data reduction used dome flat field images.
[c] Data reduction used morning twilight flat field images.

All ground-based observations were overscan corrected, bias subtracted using a master bias computed from twenty individual images, and calibrated using nightly master flat-field frames to correct pixel-to-pixel sensitivity variations. Evening twilight flats were generally used, but nights for which we utilized dome flats or morning flats are noted in Table 1. The image processing tasks were completed using basic procedures in IRAF.[10] We note that since the Jeffries et al. (2013) paper it was discovered (D. Leonard 2016, private communication) that a nonlinearity in the CCD response was present as a result of improperly set voltages on readout transistors that were used between 2008 December and 2013 November. The following correction

$$\begin{aligned}\mathrm{ADU_{cor}} = \mathrm{ADU} * (1.01353 - 0.115576 \\ \cdot (\mathrm{ADU}/32767) + 0.0296378 \cdot (\mathrm{ADU}/32767)^2)\end{aligned}$$

was applied to pixel counts on re-reduced flat field and object images (after overscan and bias subtraction) taken during that time frame using the IRAF task *irlincor*. The nonlinearity had small but noticeable effects on photometric scatter and trends within nights of data but minor effects on measured stellar characteristics.

Photometric measurements were made using the DAOPHOT II/ALLSTAR suite of programs (Stetson 1987). Because crowding was an issue for a subset of the stars, we conducted

[10] IRAF is distributed by the National Optical Astronomy Observatory, which is operated by the association of Universities for Research in Astronomy, Inc., under cooperative agreement with the National Science Foundation.

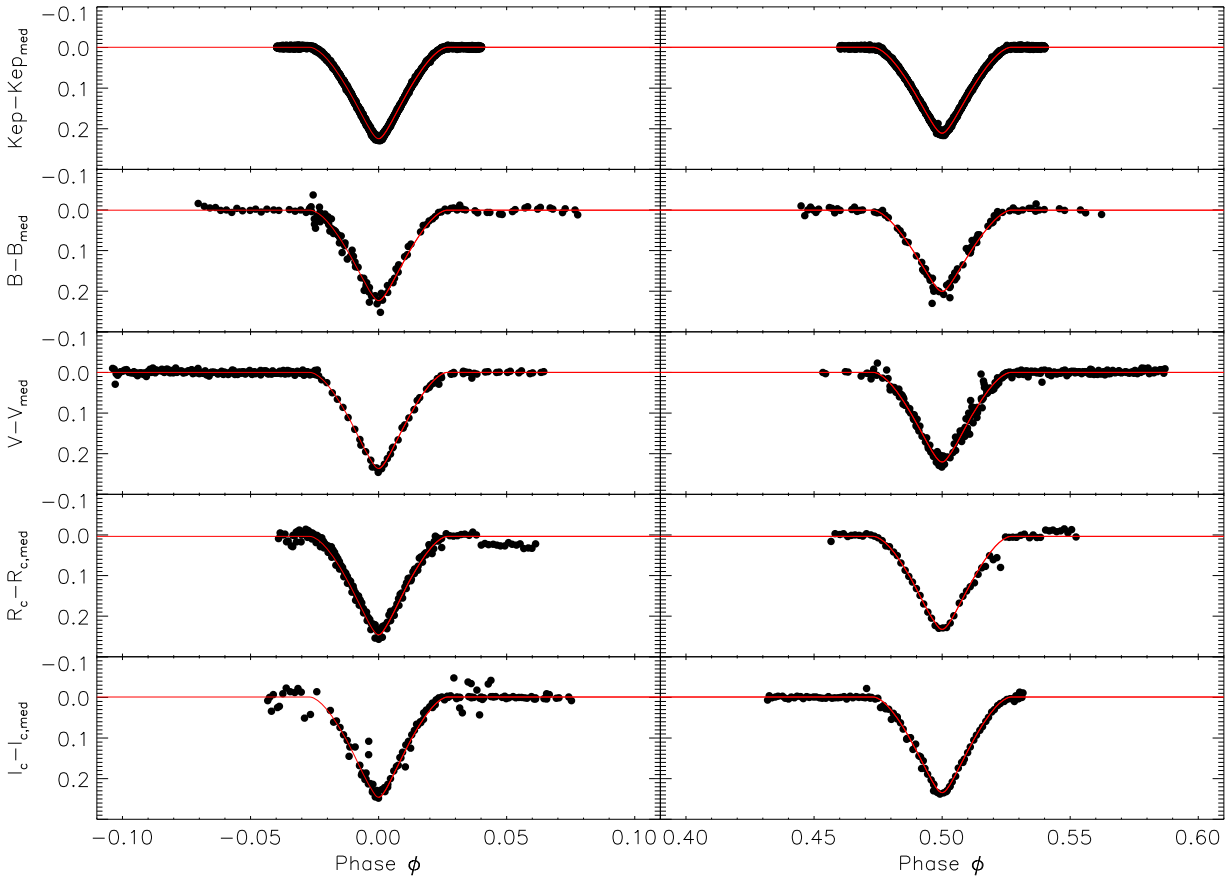

Figure 1. Photometry for WOCS 24009 from the *Kepler* spacecraft, and ground-based B, V, R_c, and I_c observations, compared with the best-fit ELC model solution (solid line) for phases in and immediately surrounding the eclipses.

point-spread function (PSF) photometry on all of the ground-based images. Typically 100–150 bright stars were chosen to determine the PSF and its variation across each frame. To improve the quality of the photometry in a differential sense, we used the observed ensemble of stars to iterate to a solution for median magnitudes of all stars and photometric zeropoints for each image (Honeycutt 1992; Sandquist et al. 2003). Figure 1 shows WOCS 24009 primary and secondary eclipse observations phased to the binary period with the slightly deeper eclipse centered on phase $\phi = 0$.

2.2. *Kepler* Photometry

The *Kepler* spacecraft made nearly continuous photometric observations of a field between Cygnus and Lyra that included NGC 6819—mission details have been previously presented in Borucki et al. (2010), Koch et al. (2010), Batalha et al. (2010), Caldwell et al. (2010), and Gilliland et al. (2010). "Super-aperture" observations of the cluster were made as part of the Kepler Cluster Study (Meibom et al. 2011). These involved a series of 20 image stamps covering the center of NGC 6819, together forming a 200 × 200 pix square field of view with 13.′25 on a side. Exposures for these stamps were taken in the long-cadence mode of 30 minutes. Eclipses of the binary components were observed using *Kepler* data for quarters 1–16, excluding quarters 6, 10, and 14 when the cluster fell on an unresponsive CCD module. We retrieved the public data from the Mikulski Archive for Space Telescopes, operated by the Space Telescope Science Institute.[11] Data processing was done using a series of Python tasks based on PyKe[12] software tools to reduce and analyze the *Kepler* simple aperture photometry. We derived times of mid-eclipse for all observable eclipses, making use of one month of short-cadence data in quarter 12 for its higher time resolution. We restricted our later analysis to photometry in and immediately around times of eclipse.

For *Kepler* photometry it is necessary to ensure that instrumental trends are removed and that contamination from other stars are accounted for. WOCS 24009 is located just outside of the center of the cluster (about 4.′4 away) but is very close to neighboring stars. With a large pixel size of 4″ across, contamination from other stars seemed likely. Contamination values as determined by the *Kepler* team ranged from 9.1% to 15.3% during different observing seasons. Even after correcting for different contamination values, cotrending the photometry against the light curves of other stars on the CCD, and fitting and removing effects from star spots, we still found significant variations in observed eclipse depths during a single quarter of observations and from quarter-to-quarter. In the end, we opted to use the short-cadence data from quarter 12 for our analysis due to the higher time resolution and in order to avoid issues of inconsistent eclipse depth from quarter to quarter. We did not apply any crowding corrections to this dataset as this

[11] http://archive.stsci.edu/kepler/kic10/search.php
[12] http://keplergo.arc.nasa.gov/PyKE.shtml

will be fit as a free parameter in the binary star models (see Section 3.2.2). The top panel in Figure 1 shows the trimmed, phased light curves of the short-cadence Kepler data.

For the triple system WOCS 40007, we followed similar procedures, deriving eclipse times (see Table 4) to measure orbit parameters for the fainter non-eclipsing star, and using short-cadence data from quarter 12 in an update of our earlier modeling of ground-based light curves (Jeffries et al. 2013).

2.3. Spectroscopy

RVs were obtained using spectra from the high-precision survey of NGC 6819 (Hole et al. 2009; Milliman et al. 2014). These spectroscopic data were taken as part of the WOCS (Mathieu 2000) using the WIYN[13] 3.5 m telescope on Kitt Peak and Hydra multi-object spectrograph instrument (MOS), which is a fiber-fed spectrograph capable of obtaining about 80 spectra simultaneously (~10 fibers set aside for sky measurements and ~70 for stellar spectra). Observations used the echelle grating with a spectral resolution ~15 km s^{-1}. Most of the spectra were centered at 513 nm with a 25 nm range covering an array of narrow absorption lines around the Mg b triplet. Spectroscopic observations for WOCS 24009 were generally completed using 2 hr integrations per visit that were split into three 2400 s integrations to allow for rejection of cosmic rays.

Image processing was done using standard spectroscopic IRAF procedures. First, science images were bias and sky subtracted, and then the extracted spectra were flat fielded, throughput corrected, and dispersion corrected. The spectra were calibrated using one 100 s flat field and two bracketing 300 s ThAr emission lamp spectra for each observation. Once the RVs were derived (see below), we also corrected for individual fiber offsets present in the Hydra MOS. A more detailed explanation of the acquisition and reduction of WOCS observations can be found in Geller et al. (2008).

2.3.1. Spectral Disentangling and Broadening Function Analysis

The spectra of WOCS 24009 are fairly complex to analyze given that there are three cluster member stars contributing absorption-line features. The brightest component does not belong to the eclipsing binary and there is substantial blending of the lines when the stars are near their eclipse times. The need to derive precise RVs in such situations led us to use broadening functions (BFs), which have been demonstrated to produce reliable measurements even for contact binaries with a great deal of rotational broadening (Rucinski 1992, 2002). BFs also minimize systematic effects on the measurements like "peak pulling" in situations where traditional techniques such as cross correlation are unable to cleanly separate the contributions from different components (Rucinski 2002).

Briefly, the BF can transform a sharp-lined synthetic or star spectrum into a broadened spectrum through a convolution. The BF contains information on how the intensity of the star's light is redistributed due to Doppler effects resulting from galactic motion, orbital motion, or rotation, among others. As a result, significant peaks in the BF give a measure of the overall RVs of the components, the function shape is an indicator of the rotation, and the total area of the peak is a proxy for luminosity in the spectral region observed.

However, even with this improvement, line blending prevented optimal determination of RVs for some epochs. As a result, we also applied the technique of spectral disentangling (González & Levato 2006). Because the spectra of the individual stars can be derived when there are a sufficient number of spectra taken with good (and differing) RV separation between the components, it is sometimes possible to derive RVs even with fairly severe line blending. Starting with initial guesses for the RVs, average spectra for the individual stars can be derived and used to subtract out the lines of all but one of the component stars in turn, and the subtracted spectra can then be used to make cleaner measurements of the RVs. The average stellar spectra and RVs can then be iteratively improved, and convergence tends to be rapid. In our case, there are three detectable stars in the spectra, and we extended the González & Levato (2006) algorithm to iteratively disentangle all three, starting with RV estimates from BF analysis of the entangled spectra.

Of the 41 spectra we had available, 34 covered wavelengths between 5000 and 5240 Å, roughly centered on the Mg b triplet, 6 covered 5460–5730 Å, and one covered 6233–6227 Å. The spectra in each group were continuum normalized before being trimmed to a common wavelength range and resampled to a common logarithmic wavelength spacing at approximately the same pixel resolution as the original spectra. Each of these groups was analyzed separately using a high-resolution solar spectrum (Hinkle et al. 2000) and IDL routines provided publicly by S. Rucinski[14] to derive the BF via singular value decomposition. The BF containing all of the singular values was then Gaussian smoothed to reduce noise—by experimenting, we found, as Rucinski has stated, that RVs were sometimes systematically offset when we used a BF that was composed from a limited set of the singular values. For the reddest spectrum, disentangling could not be used, but the BF peaks for all three components were well separated. For the bluest group of spectra, convergence was straightforward, thanks to the large number of spectra. For the mid-range group of 6 spectra, convergence was more difficult because three had very similar orbital phase ($\phi \approx 0.75$), but after restricting ourselves initially to the three spectra most widely spaced in phase for deriving the average spectra, convergence was achieved.

There were a handful of spectra for which two of the stars had RVs that were identical to within about 2 km s^{-1}, and for these disentangling failed to uniquely identify the RVs. However, by using the spectral disentangling technique, we were able to analyze a larger number of spectra than we were when using BFs alone, and could therefore derive a more complete phased RV curve. We fit Gaussian profiles to the BF peaks that could be resolved in each disentangled spectrum's BF. The central values were used to measure the stellar RVs, after corrections for fiber velocity offsets and heliocentric velocity.

In the case of the two eclipsing binary components (WOCS 24009 B and C), the stars are shown to be extremely similar in their characteristics, and so the ratio of the integrated areas of the gaussians gives us a measure of their luminosity ratio. We restricted ourselves to spectra in which three component peaks

[13] The WIYN Observatory is a joint facility of the University of Wisconsin-Madison, Indiana University, the National Optical Astronomy Observatory and the University of Missouri.

[14] http://www.astro.utoronto.ca/~rucinski/SVDcookbook.html

could be separately measured in the BF of the spectra before disentangling. This limited us to 15 of the spectra centered on the Mg b triplet, and 5 of the spectra centered on about 5595 Å. For these two groups, we found $(L_C/L_B)_\lambda = 0.863 \pm 0.033$ and 0.880 ± 0.014 (after rejection of one outlier), respectively, where the error in the mean is quoted. Because these two measurements are consistent within the uncertainties, we combined them in a weighted mean to get a final value of 0.877 ± 0.013 and we treated this as an external constraint on the V-band luminosities of the two stars in the binary star models.

The temperature difference between the bright component A and the eclipsing stars is much larger (400–500 K, versus less than 100 K for the two eclipsing stars), and so the BFs from limited wavelength ranges do not give a direct measure of luminosity ratios. However, we originally thought that this might be our only constraint on the photometric properties of component A, though this ended up not being the case (see Section 4.2.2). Using the same spectra with resolved peaks, we estimated $l_3 = L_A/(L_A + L_B + L_C)$ using the areas of the BF peaks for all three components. In the bluer region around the Mg b triplet we found 0.593 ± 0.014, and from the region around 5595 Å we found 0.534 ± 0.027. The two values differ more than they should if they were truly reflecting the light ratios in the two wavelength bands (as indicated by integrations of Coelho et al. 2005 synthetic spectra). We adopted a middle value for the ratio of the V luminosities (0.55 ± 0.02) as a loose constraint on the effects that component A's light has on reducing the measured depths of the eclipses, but the ratio was allowed to vary.

For spectra of the WOCS 40007 system, we were able to improve the precision of the measurements presented by Jeffries et al. (2013), and also make use of some spectra in which the lines of the eclipsing stars were fairly strongly blended. This allowed us to measure RVs near eclipse phases, but more importantly, it gave us new measurements of the center-of-mass velocity for the eclipsing binary that could be used to better determine the orbit of the faint non-eclipsing star (component C) in the system. Lines of component C could not be identified, so we decomposed the spectra into two components. Of the 40 available spectra, 34 were centered on the Mg b triplet, 4 covered 5460–5730 Å, and two covered 6233–6227 Å. There was not enough phase coverage to apply the disentangling method to the two smaller groups of spectra, but there was only one spectrum (in the red group) for which the BFs overlapped too strongly to separate.

Table 2 presents the measured RVs for both systems and Figures 2 and 3 show the phased RVs for WOCS 24009 and WOCS 40007, respectively, plotted over the binary orbits.

2.3.2. Photometric Temperatures

We derived temperature estimates for the stars from the BV photometry of Kalirai et al. (2001) and the VI_C photometry of Yang et al. (2013). These datasets were selected based on their high signal-to-noise observations. Comparisons with our own photometry indicated that the $B - V$ and $V - I_C$ colors in these datasets match our own calibration within about 0.005 mag even though the differences in individual wavelength bands were considerably larger. Therefore, we are reasonably certain that the color zeropoints are reliable. After correcting the colors for differential reddening using the reddening map of Platais et al. (2013) and a mean cluster reddening

Table 2
Measured Radial Velocities from the WIYN 3.5 m Telescope

mJD[a]	v_A (km s^{-1})	v_B (km s^{-1})	v_C (km s^{-1})
WOCS 24009			
2461.8591	4.14 ± 0.06	83.60 ± 0.36	−81.77 ± 0.54
2542.6483	5.89 ± 0.25	…	−23.05 ± 4.54
2840.9238	8.51 ± 0.37	77.28 ± 3.21	−91.44 ± 4.25
2857.7341	6.98 ± 0.26	−89.59 ± 1.34	83.54 ± 1.78
3190.8469	12.22 ± 0.81	46.72 ± 3.22	−51.54 ± 2.54
3576.8340	12.65 ± 0.19	−71.66 ± 1.64	62.93 ± 1.75
3810.9662	12.06 ± 0.53	…	−10.26 ± 4.77
3918.7628	12.18 ± 1.78	−38.20 ± 3.62	44.06 ± 9.46
4275.8276	10.04 ± 0.59	49.74 ± 1.65	−56.03 ± 1.16
4604.9763	8.12 ± 0.51	−50.06 ± 1.60	49.27 ± 2.17
4723.7825	5.68 ± 0.08	74.48 ± 0.68	−75.26 ± 0.70
4724.6458	8.10 ± 0.49	54.13 ± 1.77	−56.77 ± 2.76
4747.6851	6.01 ± 0.05	−86.95 ± 0.31	88.69 ± 0.45
4751.6146	8.06 ± 0.27	−82.41 ± 2.31	88.45 ± 2.16
4903.9917	6.26 ± 1.01	−23.58 ± 4.89	…
4906.0111	5.22 ± 0.13	47.62 ± 0.92	−49.27 ± 0.68
5015.9268	3.03 ± 0.26	88.69 ± 1.20	−87.61 ± 1.38
5035.8434	3.41 ± 0.07	−76.82 ± 0.41	79.37 ± 0.36
5070.6599	3.22 ± 0.12	83.90 ± 0.72	−88.06 ± 1.28
5070.7536	3.35 ± 0.09	86.37 ± 0.50	−89.49 ± 0.49
5136.6736	4.77 ± 0.05	88.94 ± 0.33	−85.92 ± 0.36
5137.6297	4.92 ± 0.40	−34.98 ± 1.00	39.05 ± 1.54
5259.9925	4.91 ± 0.07	54.15 ± 0.56	−50.28 ± 0.70
5288.8942	2.81 ± 0.25	…	…
5290.9325	4.22 ± 0.12	−37.77 ± 1.21	45.00 ± 1.20
5366.9358	3.24 ± 0.07	54.37 ± 0.47	−52.75 ± 0.52
5373.6701	2.92 ± 0.10	94.83 ± 0.91	−87.57 ± 1.07
5374.6641	2.49 ± 0.09	…	…
5374.7383	3.01 ± 0.06	…	…
5375.7362	3.63 ± 0.07	−79.28 ± 0.48	87.12 ± 0.54
5376.6635	2.86 ± 0.73	39.28 ± 2.46	−39.82 ± 2.01
5376.7375	3.06 ± 0.11	51.71 ± 0.56	−47.88 ± 0.86
5412.6967	2.48 ± 0.36	−32.48 ± 1.10	37.67 ± 1.19
5754.8363	2.63 ± 0.07	−81.39 ± 0.46	87.30 ± 0.47
5757.8027	1.64 ± 0.06	…	…
5821.8074	2.50 ± 0.12	…	…
6050.9305	1.01 ± 0.13	−72.79 ± 0.70	84.64 ± 0.74
6522.9017	1.89 ± 0.21	80.15 ± 0.91	−70.87 ± 1.33
6524.7815	−0.26 ± 0.21	−77.29 ± 2.07	87.45 ± 2.23
6527.8152	1.61 ± 0.06	…	…
6531.8955	0.06 ± 0.25	−56.86 ± 2.38	70.45 ± 1.81
WOCS 40007			
2180.6428	−39.39 ± 0.03	62.76 ± 0.05	
2415.8614	−84.48 ± 0.02	107.52 ± 0.05	
2461.7212	80.20 ± 0.02	−84.10 ± 0.05	
2475.6910	−21.15 ± 0.09	24.80 ± 0.07	
2476.8479	−50.81 ± 0.05	61.94 ± 0.04	
2856.7194	73.97 ± 0.91	−94.24 ± 1.32	
3190.6986	15.85 ± 0.03	−29.40 ± 0.10	
3191.6996	69.48 ± 0.11	−85.37 ± 0.05	
3576.8340	87.08 ± 0.05	−101.42 ± 0.19	
3577.8180	−42.06 ± 0.13	47.39 ± 0.07	
3579.8133	87.18 ± 0.09	−96.97 ± 0.10	
4345.8976	−84.59 ± 0.07	102.61 ± 0.14	
4346.6779	-9.81 ± 0.02	28.19 ± 0.17	
4367.6574	−26.91 ± 0.03	41.14 ± 0.09	
4602.9637	46.26 ± 0.05	−43.29 ± 0.04	
4603.9554	−84.65 ± 0.02	106.45 ± 0.09	
4604.9130	24.81 ± 0.03	−16.24 ± 0.04	
4605.9151	79.87 ± 0.11	−76.98 ± 0.13	
4676.6865	−35.47 ± 0.10	54.13 ± 0.07	

Table 2
(Continued)

mJD[a]	v_A (km s^{-1})	v_B (km s^{-1})	v_C (km s^{-1})
4677.6905	−52.23 ± 0.09	68.32 ± 0.15	
4715.6841	−75.07 ± 0.05	97.28 ± 0.08	
4723.7825	72.66 ± 0.02	−74.34 ± 0.11	
4747.6851	−60.32 ± 0.04	81.03 ± 0.08	
4748.6522	83.67 ± 0.04	−84.88 ± 0.03	
4749.6268	17.46 ± 0.02	−10.84 ± 0.04	
4906.0111	−31.89 ± 0.46	55.98 ± 0.86	
4906.9674	−54.41 ± 0.16	76.88 ± 0.42	
5070.7536	92.46 ± 0.13	−88.99 ± 0.25	
5071.6707	−38.03 ± 0.16	60.39 ± 0.36	
5136.6736	−1.25 ± 0.06	15.80 ± 0.09	
5259.9925	−79.46 ± 0.18	105.74 ± 0.04	
5289.9034	61.97 ± 0.05	−52.08 ± 0.11	
5365.8562	−19.52 ± 0.04	39.68 ± 0.12	
5374.7383	−81.06 ± 0.03	109.24 ± 0.04	
5376.7375	71.89 ± 0.04	−65.26 ± 0.06	
5412.6967	−64.41 ± 0.02	93.84 ± 0.02	
5413.6914	−10.15 ± 0.03	28.55 ± 0.08	
5414.6943	95.11 ± 0.03	−90.74 ± 0.05	
5440.8450	16.96 ± 0.09	−4.59 ± 0.02	

Note.
[a] mJD = BJD—2 450 000.

(This table is available in machine-readable form.)

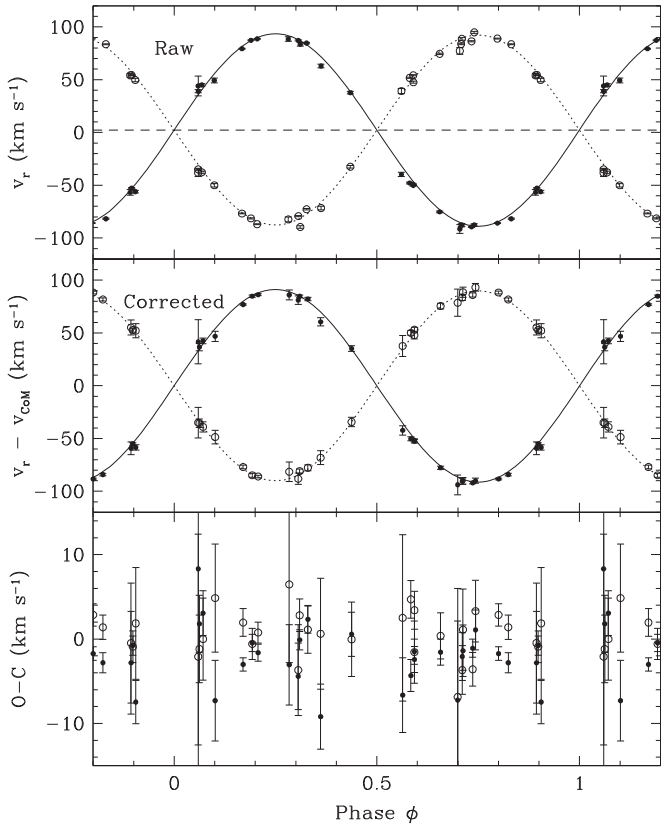

Figure 2. Top panel: raw RVs for WOCS 24009 phased to the orbital period. Model curves for the two stars are shown with solid and dotted lines. Middle panel: RVs with corrections for binary center of mass motion and for light travel time effects on the true orbital phase. Bottom panel: corrected $O-C$ diagram for the eclipsing binary components. For all panels, open circles are observations of the brighter eclipsing star and filled circles are for the fainter star.

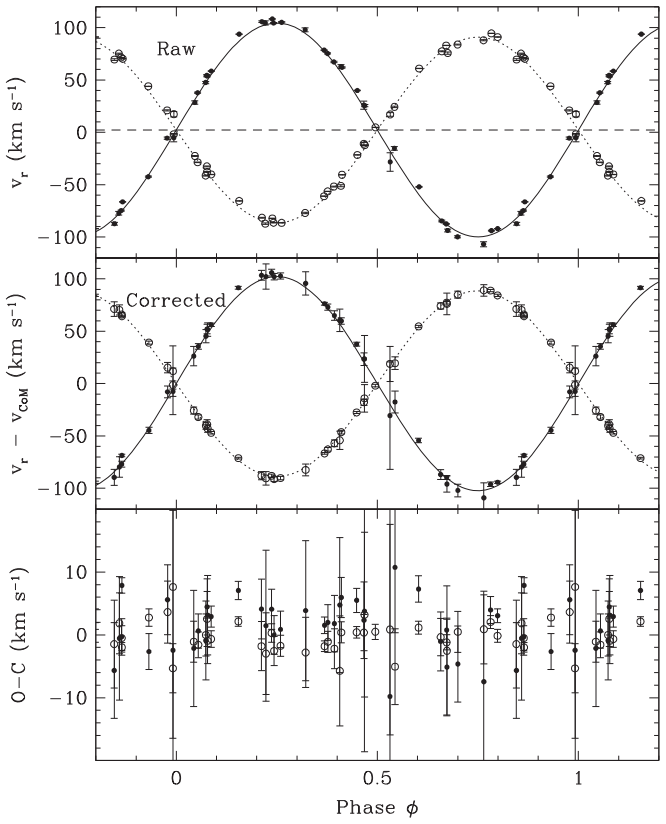

Figure 3. RVs for WOCS 40007 phased to the orbital period. In the middle panel, center-of-mass motion and light travel time corrections are applied to the RVs and phases as in Figure 2. For all panels, open circles are observations of the brighter eclipsing star and filled circles are for the fainter star.

($E(B-V) = 0.16 \pm 0.007$; Anthony-Twarog et al. 2014),[15] we applied the color–temperature relations of Casagrande et al. (2010) and averaged the temperatures derived from the $B-V$ and $V-I_C$ colors. The estimates from the two colors for each star generally agreed well with each other, although the temperatures derived from $B-V$ were about 100 K hotter on average. If we assume that [Fe/H] is subsolar, the two estimates come into better agreement.

The temperatures are given in Table 3. The stars fall into two groups with similar temperatures. The brightest star in WOCS 23009 (hereafter WOCS 23009 A; Sandquist et al. 2013a) and the brightest star in the eclipsing binary WOCS 40007 (hereafter WOCS 40007 A) are on opposite sides of the turnoff with similar colors but quite different luminosities. The stars WOCS 24009 B and C and probably WOCS 40007 B are also quite similar to each other due to their nearly identical masses.

[15] We re-examined our earlier estimation of the cluster reddening from clump stars (Jeffries et al. 2013) in light of the critique of recent measurements by Anthony-Twarog et al. (2014). We applied differential reddening corrections to our clump stars, and found that this did not change the derived reddening. However, the corrections we made to account for metallicity-dependent effects on the luminosities of the clump giants in NGC 6819 relative to those in M67 are wavelength dependent, and modifying those result in a significant change. If we assume that the difference in [Fe/H] between NGC 6819 and M67 goes from +0.09 (with NGC 6819 more metal-rich) to 0, our derived reddening goes from $E(B-V) = 0.12$ to 0.15. While this is not proof that the larger value is correct, it does show that the different estimations of reddening may be consistent. If the metallicity difference between M67 and NGC 6819 is established to be closer to 0, the higher reddening value should be preferred.

Table 3
Measured Parameters for Stars in NGC 6819

Star ID	V^a	$B-V^a$	$T_{\rm eff}$ (K)	$M/M_\odot$	$R/R_\odot$	$(m-M)_V$
WOCS 23009 A	15.130	0.632	6315	1.464 ± 0.011[b]	2.149 ± 0.009	12.39 ± 0.07
WOCS 40007 A	16.111	0.642	6350	1.218 ± 0.008	1.367 ± 0.003	12.40 ± 0.08
WOCS 40007 B	16.949	0.692	5900	1.068 ± 0.007	1.090 ± 0.002	12.40 ± 0.08
WOCS 24009	15.214	0.661	⋯	⋯	⋯	⋯
WOCS 24009 A	15.743	0.589	⋯	1.251 ± 0.057	⋯	⋯
WOCS 24009 B	16.835	0.721	5925	1.090 ± 0.010	1.099 ± 0.006 ± 0.005[c]	12.37 ± 0.07
WOCS 24009 C	16.965	0.744	5855	1.075 ± 0.013	1.069 ± 0.006 ± 0.013[c]	12.37 ± 0.07

Notes.
[a] The quoted photometry is from Kalirai et al. (2001), but has not been corrected for zeropoint differences in calibration or for differential reddening.
[b] Based on a photometry-based extrapolation from other eclipsing stars in the cluster.
[c] The two uncertainties are estimates of the random and systematic effects with the systematic uncertainty estimated from the scatter in the three models in Table 6.

3. ANALYSIS

3.1. Cluster Membership

The information extracted from models of WOCS 24009 will only be of use for assessing the properties of NGC 6819 if WOCS 24009 is a member of the cluster. There are three ways in which cluster membership can be examined. First, the most restrictive evidence for cluster membership comes from proper-motion measurements (Platais et al. 2013). The proper motions are derived from a combination of old photographic plates with CCD observations obtained from the 3.6 m Canada–France–Hawaii Telescope. For WOCS 24009 (star 592928 in Platais et al. 2013), the formal uncertainty of proper motion in either axis is slightly less than 0.2 mas yr^{-1} and the star's offset proper motion from the cluster mean motion is also ∼0.2 mas yr^{-1}. These parameters yield an astrometric membership probability of 99%. We can also compare the systemic RV to those measured for other stars in the field to determine membership. Milliman et al. (2014) have done an extensive RV survey of stars in the NGC 6819 field, and they use one-dimensional Gaussian fits to the field $F_f(v)$ and cluster $F_c(v)$ velocity distributions to compute a membership probability:

$$p(v) = \frac{F_c(v)}{F_f(v) + F_c(v)}$$

Ideally, we would calculate this from the system velocity (γ) derived from a three-body solution to the stellar orbits (see Section 3.2.1). However, the system has not been observed over a large enough fraction of the outer orbit period to properly determine γ. The velocity at which component A and the binary center-of-mass velocities cross is approximately 2 km s^{-1} though, consistent with the cluster mean RV of 2.45 km s^{-1} (Milliman et al. 2014). This also supports membership. The last method we considered uses the position of the system in relation to the core radius of the cluster, where r_c is a King model value (1.8 r_c; Kalirai et al. 2001). A membership probability is estimated as 45% using a ratio of the spatial density of probable cluster members to the total spatial density, but this method only weakly constrains the membership because it does not take into account differences in the cluster and field distributions in the CMD. Other evidence that supports cluster membership are the physical similarities between WOCS 24009 eclipsing binary stars and the well-measured stars in WOCS 40007 (Jeffries et al. 2013), for which the membership information is more complete. Based on the evidence available to date, we find no reason to doubt that WOCS 24009 is a cluster member.

3.2. RV and Light-curve Modeling

Three stellar components were identifiable in spectra taken of WOCS 24009 even before the *Kepler* mission began. However, due to the similar characteristics of the fainter two stars and significant blending with the brightest component in many spectra, an orbital solution had not been determined. The *Kepler* photometry not only made it possible to differentiate between the two eclipses of very similar depth, but the eclipse timings also showed clear evidence of a light travel time (LTT) effect resulting from the gravitational influence of a third star on a wide orbit. It also became clear that scatter in the RVs of the eclipsing stars was being introduced by reflex motion of the binary in response to the motion of component A. The eclipse timings are given in Table 4 with the earliest eclipse observed from the ground in 2001 July (Talamantes et al. 2010).

We therefore sought a consistent solution assuming that the system is hierarchical: the eclipsing stars in the binary follow Keplerian orbits, and component A and the barycenter of the binary also follow much larger Keplerian orbits. The modeling of the stars was therefore separated into two parts: characterization of the RV curve of the eclipsing binary and the wide orbit of the component A using the RVs and eclipse timings, and characterization of the light curves to derive final masses and radii for the eclipsing stars.

Models for the photometric and RV measurements were computed using the ELC code (Orosz & Hauschildt 2000). ELC uses a χ^2 statistic to determine the goodness-of-fit where the overall χ^2 is the sum of the χ^2 for each photometry filter, RVs for each binary component, and any observational constraints. Genetic and Markov chain optimizers were used to determine best-fit models in the multi-dimensional parameter space. We generally began with the genetic algorithm in order to search large volumes of parameter space to arrive at the best fit minimum for each binary parameter. After the initial identification of a best fit, the uncertainties on individual photometric and RV observations were scaled in order to produce a reduced χ^2 of 1. This is essentially equivalent to replacing the a priori uncertainty estimates with a posteriori estimates that can account for random systematic effects. Subsequently, we used Markov chain Monte Carlo modeling (Tegmark et al. 2004) to determine the solution and search alternative models near the parameter minima to estimate

Table 4
Eclipse Timings

BJD—2450000	σ	Eclipse	Notes
		WOCS 24009	
2104.86904	0.00027	P	R_c ground
4697.66460	0.00033	S	$R_{\rm Kron}$ ground
4965.88626	0.00025	P	Beginning of Kepler Q1
4967.71076	0.00019	S	…
4969.53563	0.00022	P	…
4971.36016	0.00017	S	…
4973.18516	0.00017	P	…
4975.00933	0.00025	S	…
4976.83423	0.00008	P	…
4978.65877	0.00024	S	…
4980.48360	0.00020	P	…
		WOCS 40007	
2102.88901	0.00008	P	R_c ground
4623.88162	0.00015	S	V ground
4698.73250	0.00011	P	$R_{\rm Kron}$ ground
4964.69147	0.00025	S	Beginning of Kepler Q1
4966.28385	0.00023	P	…
4967.87663	0.00019	S	…
4969.46896	0.00013	P	…
4971.06181	0.00005	S	…
4972.65416	0.00012	P	…
4974.24685	0.00022	S	…
4975.83930	0.00022	P	…

(This table is available in its entirety in machine-readable form.)

parameter uncertainties. 1σ uncertainties were found by identifying the parameter ranges covered by solutions that had a χ^2 (not reduced χ^2) value within 1 of the minimum (Avni 1976).

3.2.1. Orbit Modeling of Third Star

When modeling the RVs and eclipse timings for WOCS 24009, we conducted simultaneous fits for the following parameters: period $P_{\rm bin}$ and time of primary eclipse $t_{\rm bin}$ for the eclipsing binary (in its comoving reference frame); period P_A, time of periastron t_A, eccentricity e_A, and argument of periastron ω_A for the third star's orbit; the RV amplitudes for the third star K_A and the stars in the eclipsing binary (K_B and K_C), and the RV of the barycenter of the system γ. However, it became clear that some aspects of the third star's orbit are not well constrained with the current data. The basic problem is that, even though we have data covering approximately 4000 d, by chance we have observed component A orbit essentially between times of zero RV with one velocity maximum (closest to periastron) in between. Because of the distribution of the observations, there are correlations between the system velocity, the velocity semi-amplitudes of the third star K_A and binary $K_{\rm bin}$, and the eccentricity.

Because the indications are that the system is a member of NGC 6819, we fixed the system velocity to the cluster average (Milliman et al. 2014). This choice may introduce systematic errors into the values of K_A and K_B, but there are good reasons for trying to model the third star's orbit as best we can right now. First, we can correct the binary star velocities to first order for the motion induced by component A, producing more precise measurements of the velocity amplitudes K_B and K_C, and thus the masses of the stars. The RVs of the eclipsing stars are directly affected by the center-of-mass motion, but LTT also affects the inferred phase of each observation. This effect is relatively important in this system (at the 0.01 level in phase) because of the large size of the third star's orbit and the relatively short period of the eclipsing binary. The top two panels of Figure 2 illustrate the RV variations with and without the corrections to the RVs and phases of each observation. Second, the ratio of the velocity amplitudes allow us to determine the mass ratio $M_A/(M_B + M_C)$, and in principle, the mass of the third star. The size of the third star cannot be determined because there is no evidence that component A eclipses either binary component in *Kepler* photometry. However, our photometric decomposition indicates that the third star is the one closest to the cluster turnoff with a *measurable* mass, in spite of the lack of eclipses.

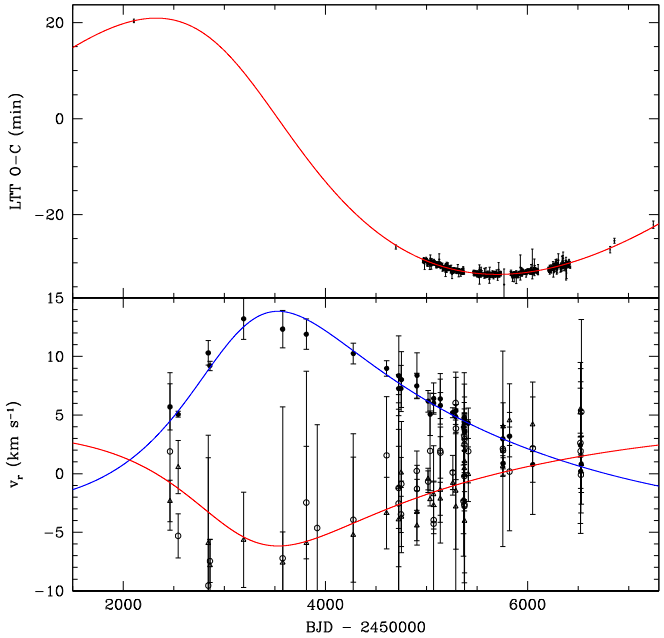

Figure 4. Orbit modeling solutions for the third star in WOCS 24009, plotted to fit the RVs and eclipse timings as described in Section 3.2.1. Top panel: $O - C$ for variations in binary eclipse timings. Bottom panel: observed RVs of the bright third star WOCS 24009 A (solid) and binary star components (open) after subtracting binary star model predictions. Binary star model curves are shown for the third star (blue) and binary barycenter (red).

Figure 4 shows the results of our best preliminary fit to the eclipse timings and RVs. The top panel shows the variations in the binary star eclipse timings compared to a linear ephemeris (observed minus computed: $O - C$) over time. The error bars are scaled to give a reduced χ^2 of about 1 for the RVs and LTT separately. This was needed to ensure that neither dataset was weighted too heavily in finding a joint solution. The bottom panel shows observed RVs of the binary center of mass and the third star.

To obtain this fit, we had to apply some constraints based on an analysis of the observations. Extrema in the top plot of the eclipse timings correspond to times when the binary center-of-mass velocity crosses the barycenter velocity γ, and these are well constrained by the RV observations. The first several RV observations (BJD before 2453000) indicate that the crossing occurred around BJD 2452100–2452300, very close to the first ground-based eclipse observation (BJD 2452105). Similarly, the observations by *Kepler* have covered the LTT minimum (near BJD 2455900), as corroborated by the RVs. As a result, the full LTT amplitude is constrained to be close to 56 minutes. The eccentricity of the outer orbit is clearly visible in the

Table 5
Orbit Solution for the Binary Stars in WOCS 24009 and WOCS 40007

Parameter	WOCS 24009		WOCS 40007	
	This Study	Milliman et al.	This Study	Milliman et al.
$P_{\rm bin}$ (d)	3.6493010 ± 0.00000018	3.64921 ± 0.00004	3.18509586 ± 0.00000008	3.185087 ± 0.000012
P_3 (d)	8333 ± 30	⋯	3248 ± 3	⋯
$t_{\rm bin}$ (HJD—2450000)	2104.85489 ± 0.00017	4836.1 ± 1.4	2102.88690 ± 0.00004	4329.3 ± 2.4
t_3 (HJD—2450000)	3182 ± 13	⋯	5601.3 ± 2.5	⋯
e_3	0.368 ± 0.003	⋯	0.307 ± 0.002	⋯
i_3 (°)	68.7	⋯	⋯	⋯
ω_3 (°)	145.0 ± 0.6	⋯	72.4 ± 0.3	⋯
$K_{\rm bin}$ (km s^{-1})	4.74 ± 0.02	⋯	4.764 ± 0.009	⋯
K_A (km s^{-1})	8.21 ± 0.35	⋯	88.9 ± 0.4	87.9 ± 1.0
K_B (km s^{-1})	88.86 ± 0.51	88.0 ± 1.3	101.6 ± 0.3	103.3 ± 1.1
K_C (km s^{-1})	90.05 ± 0.35	90.0 ± 1.3	⋯	⋯
$q_{\rm bin} = M_2/M_1$	0.987 ± 0.007	1.023 ± 0.023	0.875 ± 0.005	0.851 ± 0.014
$q_A = M_A/(M_B + M_C)$	0.578 ± 0.026	⋯	⋯	⋯
γ (km s^{-1})	3.17 ± 0.12	0.4 ± 0.7	2.83 ± 0.18	3.7 ± 0.5

asymmetry of the RVs between the zero crossings. Note that the RV curve for the eclipsing binary is related to the derivative of the eclipse timing curve, with the RV extrema occurring at inflection points in the LTT curve. Unfortunately, the period of the third star's orbit will not be constrained more tightly until more eclipse times are measured as the eclipsing binary moves more rapidly away from us. We are also unable to directly measure the RV amplitudes because both velocity extrema have not been observed and because the precise system velocity for the triple is not well constrained yet.

The best current fit for the eclipsing binary orbit is given in Table 5. For comparison, we include the RV fits from Milliman et al. (2014). We expect our results to be more precise and accurate on account of the improvements in technique for deriving the RVs from the complex spectra and, more importantly, due to our control for the effects of the third star. In the important case of the velocity semi-amplitudes for the eclipsing stars $K_{B,C}$, a comparison shows that there are systematic differences in values by approximately 1σ compared to the Milliman et al. fits, and a significant decrease in uncertainty by a factor of 2–3. The lower K uncertainties translate to a corresponding reduction in the uncertainties in the derived masses. With the fit for the third star's orbit in hand, we can compensate for its effects on the binary RV measurements. These values are used as constraints in our models of the eclipsing binary light curve (see Section 3.2.2). Using the mass ratio from this analysis ($q_{\rm bin} = 0.987 \pm 0.007$), we can determine center-of-mass velocities for the eclipsing binary at each epoch, and use them to measure the mass ratio $q_A = M_A/(M_B + M_C)$. Using the weighted average of the eight best measurements near the velocity extremum (BJDs 2452461 to 2454747), we derive a value $q_A = 0.578 \pm 0.026$.

The calculated masses for the three stars are presented in Table 3. We calculate the mass of the third star (WOCS 24009 A) to be $M_A = 1.251 \pm 0.057\,M_\odot$. The inclination of its orbit can be estimated using Kepler's third law and the masses and period, either by comparing the expected RV amplitudes to the measured ones or by comparing the expected size of the orbit to the amplitude of the LTT effect on the eclipses (which is related to the projection of the orbit along the line of sight). At present, the LTT amplitude is much better constrained than the RV semi-amplitudes for the binary $K_{\rm bin}$ and third star K_A. So using the LTT results, we estimate the inclination to be $i_A = 68°$. Because the inclination is quite far from edge-on, the third star will not eclipse and its radius cannot be measured directly. The most important information it will provide will come from its mass and good photometry. Three-body (non-Keplerian) dynamics could affect how precisely we are able to determine the characteristics of the third star's orbit, especially when all of our observations span approximately one orbital period. However, some exploratory calculations (D. Short 2016, private communication) indicate that the effects are likely to be quite small as a result of the large difference in orbital periods. The difficulties involved in measuring the motions of the binary center of mass and the third star means that the third star's mass will not be a strong constraint on cluster properties at present. Future monitoring should bring down the mass uncertainty significantly.

Finally, because additional *Kepler* observations were available and because we improved our analysis of the RV measurements for the WOCS 40007 binary (Jeffries et al. 2013), we have updated our models of that triple system. Its third star is considerably fainter than the eclipsing binary, so that we are unable to measure its RVs from spectra and will not be able to derive its mass. However, improved models of the third star's orbit will allow us to reduce the mass uncertainties for the eclipsing stars. The combination of RVs and eclipse timings has given us observations covering more than one complete orbit of the third star, although with differing degrees of precision. The improved RVs more clearly draw out the shape of the velocity curve, and have significantly increased the measured eccentricity. The additional *Kepler* eclipse timings have allowed us to precisely identify both inflection points in the LTT O-C diagram, which in turn determines the duration of the RV swing from maximum to minimum. The velocity semi-amplitudes for the eclipsing binary have not changed greatly since our original determination, but the uncertainties have improved by about a factor of two. An updated plot of the third star's orbital effects is shown in Figure 5.

3.2.2. Binary Star Modeling

Before we started to fit the light curves with binary star models, we trimmed the photometric data to observations taken in and near eclipses. *Kepler* photometry shows that there is negligible variation outside of eclipse, indicating that ellipsoidal variations (due to non-spherical stars) and reflection effects

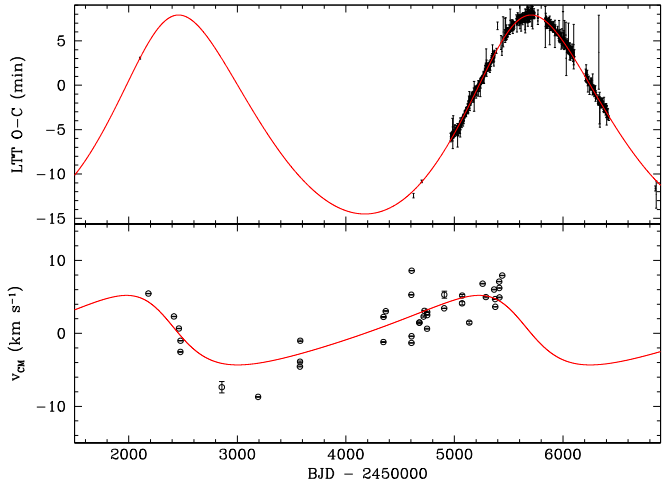

Figure 5. Orbit solution for the third star of WOCS 40007, similar to Figure 4. Top panel: $O - C$ for variations in binary eclipse timings. Bottom panel: observed RVs of the eclipsing binary center of mass compared with model predictions.

can be ignored. Variations in the out-of-eclipse photometry (due to systematics in the *Kepler* photometry or atmospheric effects in the ground-based photometry) added unconstructively to the χ^2 of our fits, and substantially lengthened the time needed to compute model fits, so we expunged these points. We also applied zeropoint offset corrections to nights of ground-based data, where the offset was determined from the median magnitude of any out-of-eclipse data from that night. These corrections were made to bring the ground-based light curves into greater consistency, and are likely to be the result of stellar activity. Most of the nights only had out-of-eclipse photometry available either from the evening or morning, so the median magnitude was taken for that and applied to the whole night. For nights with out-of-eclipse data on both sides of the eclipse, the median magnitude was determined using the side with the largest number of datapoints and least uncertainty in the magnitudes.

The effects of limb-darkening were examined by fitting the data with two different types of models: one using a quadratic limb-darkening law, and the other using PHOENIX model atmospheres (Hauschildt et al. 1997). When using a quadratic limb-darkening law, we computed models using *Kepler* data both with and without our ground-based observations. In both types of models we fixed one coefficient in the *Kepler* filter band for each star using ATLAS atmosphere values from Claret (2000) and fitted for the other, which allowed ELC greater freedom to search for the coefficient values for each filter that produce the best fits to the light curves. By fixing one coefficient and fitting for the other, systematic error in the assumed coefficient (due to incorrect $T_{\rm eff}$, log g, or metallicity) can be partly compensated for because coefficients tend to be correlated. With the more precise *Kepler* data, the coefficient is better constrained than in the ground-based data. Finally, because PHOENIX model atmospheres describe the limb darkening of the stars and variation of emitted intensity with emergent angle, there is no need to assume limb-darkening coefficients. On the flip side, systematic errors in the atmosphere models can introduce systematic errors in best-fit parameters. We have computed models using both limb darkening descriptions as a way of assessing the systematic uncertainties and their effects on the measured stellar characteristics.

Results for the two types of models can be found in Table 6. We fit for 10 free parameters in the light curve models: inclination i, ratio of the brightest eclipsing star radius to the semimajor axis R_B/a, ratio of radii of the eclipsing stars R_B/R_C, temperature of the brighter eclipsing star T_B, ratio of the temperatures of the eclipsing stars T_C/T_B, temperature of the third star T_A, ratio of the surface area of the bright component A to the surface area of the brightest eclipsing star R_A^2/R_B^2, binary mass ratio $q = M_C/M_B = K_B/K_C$, velocity semi-amplitude of the brightest eclipsing star K_B, and external contamination of the *Kepler* light curve. *Kepler* photometry provides a very tight constraint on the shape of the light curves, but not their absolute depths due to the contamination by unassociated stars projected near WOCS 24009 on the sky. Our ground-based data, which is much less affected by contamination from unassociated stars, provides better constraints on the absolute depths of the eclipses.

We have applied the following spectroscopic constraints to the light curve models during the fits: temperature of the third star T_A, the luminosity ratio for the eclipsing stars L_C/L_B, velocity semi-amplitude K_B, and binary mass ratio $q = K_B/K_C$. q, K_B, and T_A are included as free parameters to allow their values to vary within the uncertainties of the triple star fit and spectroscopic temperature measurement in order to incorporate this uncertainty in the overall uncertainty for the computed binary parameters.

4. RESULTS AND DISCUSSION

Before we begin a discussion of the cluster age, it is necessary to discuss recent constraints on the cluster's metallicity. Until recently, the only direct measurement of the composition was Bragaglia et al. (2001): [Fe/H] = +0.09 from three red clump stars. However, additional measurements have become available. Anthony-Twarog et al. (2014) used Strömgren photometry to derive [Fe/H] = -0.06 ± 0.04. While this result does depend somewhat on the reddening, this can be derived from the photometry for individual stars and combined to get a robust cluster average, and the authors did a thorough job of examining quality issues that could have affected their zeropoints. The APOGEE experiment has also been taking infrared spectra of a large sample of mainly red giants and red clump stars, including observations in the *Kepler* field. NGC 6819 is one of the clusters being used to calibrate stars of near solar metallicity, and the metallicities derived from comparisons with synthetic spectra are being corrected to match literature values. That said, APOGEE has provided their uncalibrated abundance values, which have been lower than their calibrated values by 0.03–0.05 dex. For example, Mészáros et al. (2013) derived an uncalibrated [M/H] = +0.02 for NGC 6819 using data from Data Release 10. We extracted measurements for 34 stars identified as asteroseismic members in Stello et al. (2011) from Data Release 12, and find +0.09 for both the uncalibrated [M/H] and for [Fe/H] specifically. (The calibrated value of [M/H] is 0.05 dex higher.) APOGEE abundances are not determined truly differentially with respect to the Sun: they use Asplund et al. (2005) solar abundances (with $Z_\odot = 0.0122$) as a reference for producing synthetic stellar models. More recent compilations have a higher solar abundance. For example, if $Z_\odot = 0.0134$ (Asplund et al. 2009) was used instead, it would

Table 6
Orbital Solutions: Limb-darkening Law

Parameter	Kepler + Ground	Kepler Only	Model Atmospheres
Constrained: All Runs			
t_o (HJD—2450000)		2104.8424 ± 0.0002	
P (d)		3.64930279 ± 0.00000016	
$q = M_C/M_B$		0.987 ± 0.007	
K_B (km s^{-1})		88.86 ± 0.54	
L_C/L_B		0.877 ± 0.013	
T_A (K)		6330 ± 53	
Fitted:			
i (°)	89.27 ± 0.02	89.28 ± 0.02	89.42 ± 0.02
R_B/a	0.0853 ± 0.0002	0.0853 ± 0.0001	0.0856 ± 0.0002
R_B/R_C	1.029 ± 0.003	1.025 ± 0.003	1.020 ± 0.003
T_C/T_B	0.988 ± 0.0002	0.988 ± 0.0002	0.989 ± 0.0002
R_A^2/R_B^B	2.126 ± 0.024	...	2.071 ± 0.023
Contam	0.047 ± 0.003	0.070 ± 0.003	0.053 ± 0.003
Derived:			
R_B ($R_\odot$)	1.099 ± 0.006	1.100 ± 0.007	1.104 ± 0.007
R_C ($R_\odot$)	1.069 ± 0.006	1.073 ± 0.007	1.083 ± 0.007
R_C/a	0.0829 ± 0.0002	0.0832 ± 0.0002	0.0839 ± 0.0001
$(R_B + R_C)/a$	0.1682 ± 0.0002	0.1684 ± 0.0002	0.1695 ± 0.0001
$a(R_\odot)$	12.90 ± 0.07	12.90 ± 0.08	12.90 ± 0.08
log g_B (cgs)	4.392 ± 0.003	4.392 ± 0.003	4.389 ± 0.003
log g_C (cgs)	4.411 ± 0.003	4.408 ± 0.003	4.400 ± 0.003

result in a lower zeropoint for the APOGEE metallicity scale by about 0.04 dex. Finally, Lee-Brown et al. (2015) presented high-dispersion abundance analysis of a large sample (more than 240) of likely single cluster members determined differentially with respect to solar spectra. Their quoted values are [Fe/H] = −0.03 ± 0.06 for the whole sample, and their preferred value −0.02 ± 0.02 for a subsample of main sequence stars.

To determine a most likely range of metal contents to use in comparisons with models, we must consider both the differences in measured [Fe/H] and the lingering uncertainty in the solar metal abundance $Z_\odot$. The value of $Z_\odot$ affects the APOGEE abundance for NGC 6819 as described above, but different sets of isochrones also assume different values. It is safest to compare isochrones with the same Z, rather than [Fe/H] if we are to avoid unnecessarily obscuring real physics effects. The values of $Z_\odot$ in recent analyses go from 0.0134 (Asplund et al. 2009) to 0.0153 (Caffau et al. 2011)—still a significant source of uncertainty. We believe that the best range for NGC 6819 comparisons goes from $Z = 0.012$ (using the Lee-Brown et al. 2015 measurement of [Fe/H] ≈ −0.03 and $Z_\odot = 0.0134$) up to $Z = 0.015$ (using APOGEE abundances for their assumed $Z_\odot$). The ratio of these two values corresponds to approximately a 0.1 dex difference in [Fe/H].

4.1. Interactions Within the WOCS 24009 and 40007 Eclipsing Binaries

If we are going to use the binaries of NGC 6819 to constrain the cluster age, we need to be certain that interactions have not modified the stellar characteristics significantly. While the eclipsing binaries WOCS 24009 and WOCS 40007 are detached and have not exchanged mass, they are close enough that there are legitimate concerns about the effects of tidal interactions. For well-measured short period (0.6–2.8 day) binaries with masses in the range 0.8–1.1 $M_\odot$, it has been seen that stars sometimes appear larger by 10%–20% than predicted by single-star evolutionary models (Clausen et al. 2009). To explain what is physically occurring inside stars with radii that are larger than expected from theory, Torres et al. (2006) suggested that synchronized rotation in short-period binaries leads to magnetic field production and increased chromospheric activity (Chabrier et al. 2007). For stars with masses of about a solar mass or less, the magnetic activity can affect the flow of energy through the convective envelope by reducing the efficiency of convective heat transport forcing the star to grow larger to compensate. Torres et al. also showed that stars with anomalously large radii can be modeled with the same age as their companion if a lower mixing length parameter is used. Most longer period binaries show little or no evidence of anomalies, but the transition range of periods is ill-defined.

The two close detached binaries we discuss in this paper have periods in the sparse 3–4 day range: WOCS 40007 ($P = 3.185$ days; Jeffries et al. 2013) and the current subject WOCS 24009 ($P = 3.65$ days). These binaries carry the added benefit that they are members of a cluster with an externally constrained age and a fairly well determined chemical composition, giving us a better theoretical idea of what the stellar characteristics should be. Therefore these systems can extend our understanding of the causes of stellar inflation.

Jeffries et al. found some indication that the radius of WOCS 40007 B is larger than expected from models with the spectroscopic composition (Bragaglia et al. 2001) and preferred age of 2.5 Gyr, but at the time the precision of the mass measurement prevented this from being a strong statement. They considered the possibility that perhaps the adopted

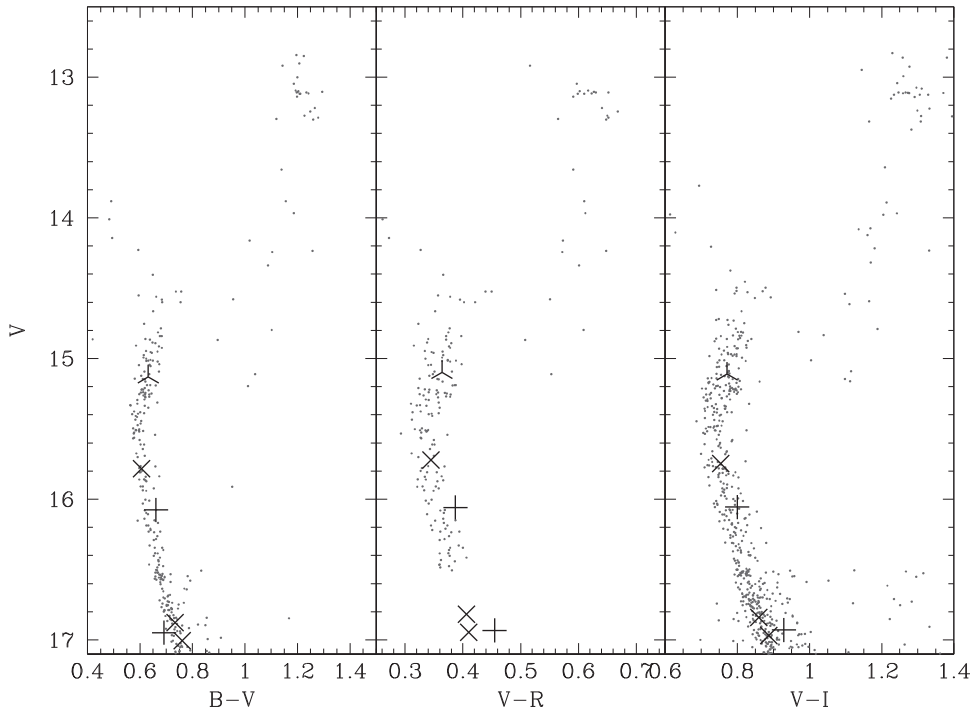

Figure 6. CMDs for NGC 6819 in $B - V$ (Kalirai et al. 2001), $V - R_c$ (Hole et al. 2009), and $V - I_c$ (Yang et al. 2013). The sample has been restricted to likely members, but has not been adjusted otherwise. The components of the eclipsing binaries WOCS 23009 (three-point star), WOCS 24009 (×), and WOCS 40007 (+) are shown.

metallicity or some other composition variable (most importantly, helium) was offset from the cluster value. They examined models with decreased metallicity that produced a slightly better consistency between the ages implied by both eclipsing stars in WOCS 40007. Ages implied by the lower metallicity were lower by about ∼0.2 Gyr and were more consistent with ages derived from the CMD fits. However, with the improvement of the mass measurements for WOCS 40007, the differences between observations and models are considerably more significant, and radius inflation may be necessary to explain the characteristics of component B, and possibly both stars.

The eclipsing stars of WOCS 24009 provide an empirical basis for judging the radius of WOCS 40007 B—the masses of the stars are similar (so they should have comparable internal stellar structure), and they were formed in the same cluster (so that their initial chemical compositions should be identical). However, WOCS 24009 has a longer period, and should show somewhat weaker evidence of rotationally induced activity. Indeed, we find that the radii of WOCS 40007 B and WOCS 24009 B and C are very similar even though WOCS 40007 B is 0.02–0.03 $M_\odot$ smaller in mass. So there is some indication that the radius of WOCS 40007 B is inflated by a few percent.

Results for other close binaries provide additional perspective. Detached systems with solar-type stars and periods shorter than 3 d (e.g., EF Aqr; Vos et al. 2012) are generally circularized, leading to rapid rotation ($v \sin i$ = 20–73 km s^{-1}) synchronized with the orbit. These binaries generally have at least one component with a radius measurement about 10% larger than expected from models, show signs of induced magnetic activity in the form of X-rays, have Ca II H and K lines in emission, and light variations attributed to starspots. On the other hand, binaries with periods as short as 6.94 days (EW Ori, Clausen et al. 2010) show good agreement with standard models of solar-type stars. One other system with a period between 3 and 7 days contains a lower-mass star with significant radius inflation (V636 Cen: $P = 4.3$ days, $M_2 = 0.854 \pm 0.003\,M_\odot$; Clausen et al. 2009), but the orbits in that system are significantly eccentric ($e = 0.135$) and the stars rotate pseudosynchronously with the orbit.

The larger period of WOCS 24009 compared to WOCS 40007 probably has a relatively small effect itself—it probably means that the rotational velocities of the stars in WOCS 24009 are lower by about 15%. If the WOCS 24009 stars are rotating synchronously with their orbit, the equatorial rotation speed should be about 15 km s^{-1}. Probably more important is the larger mass of the WOCS 24009 stars. Even though the mass difference is small, this means that the convective envelopes are less massive by as much as a factor of 2 (for example, see Figure 16 of Torres et al. 2006) between WOCS 40007 B and WOCS 23009 A, and the radial extent of the convective zones are reduced by an even greater factor. These differences might be expected to reduce the effects of magnetic activity more drastically.

The photometry of WOCS 40007 B can be decomposed accurately from the other two stars thanks to the total eclipses. Using the eclipse depths we derived in BVR_cI_c, we can put component B in different CMDs, as seen in Figure 6. When $B - V$ color is used, component B falls slightly to the blue of the main sequence, but in $V - R_c$ and $V - I_c$ colors, component B falls significantly to the red of the main sequence. This also holds true for a comparison with the WOCS 24009 eclipsing stars as well. Checking the dates of the calibrating observations for the sources (Kalirai et al. 2001 for $B - V$, Hole et al. 2009 for $V - R_c$, and Yang et al. 2013 for $V - I_c$), we see no reason to believe that the CMD photometry for WOCS 40007 was affected by eclipses. According to the reddening map from Platais et al. (2013), WOCS 40007 is in a slightly more heavily

reddened portion of the cluster field. This can partly explain the red positions of WOCS 40007 B in $V-R_c$ and $V-I_c$, but we do not have an explanation for the bluer position in $B-V$.

A remaining question is whether the even more massive star WOCS 40007 A has had its radius affected. When the more massive star in a short period detached binary is expected to have a very low mass convective envelope, the radius generally agrees better with standard stellar models (e.g., FL Lyr, Popper et al. 1986; V1061 Cyg, Torres et al. 2006). However, in field binaries, modest increases in radius can be disguised as larger ages if the age is not otherwise constrained, as it is in clusters (see V375 Cep in the cluster NGC 7142; Sandquist et al. 2013b). The convective envelope of WOCS 40007 A is theoretically expected to be less massive than those in the WOCS 24009 stars by another factor of more than 2. A combination of somewhat larger than average reddening for WOCS 40007 and a correction for the contribution of the faint third star is able to shift the brighter eclipsing star into the middle of the main sequence band. Because the three stars appear to share the same mass–radius isochrone, we will treat WOCS 40007 A as probably unaffected by the interaction with its companion.

To further study the connection between chromospheric activity and stellar size, more examples of well-studied binaries in the suggested mass range with accurately measured mass, radius, and temperature will be needed to map out the dependence of radius inflation on orbital period/rotational velocity and stellar mass/convection zone depth. In the sample of eclipsing stars in NGC 6819, component B in WOCS 40007 shows the strongest evidence of tidal inflation as a result of the interaction with its companion component A, but additional work on the eclipsing binaries will be needed to improve the significance of the comparison.

4.2. Photometry of the Component Stars

Part of the effort in this paper has been to incorporate all of our results for the eclipsing binaries of NGC 6819 into a better overall constraint on the characteristics of the star cluster. Because the photometry of individual stars (in conjunction with their masses) contains precision information that can contribute to age determination, we discuss our procedure for decomposing the light of the different multiple star systems into each component.

4.2.1. WOCS 40007

The total eclipse of WOCS 40007 B gives us a precise means of separating the light of component B. We remeasured the eclipse depths after the re-reduction of the ground-based photometry described in Section 2.1. We only included nights for which we could measure both the eclipse minimum and out-of-eclipse levels. The results are shown in Table 7, and the resulting magnitudes for component B are shown in Table 3. The light of component A and the faint third star cannot be as precisely disentangled. We drew magnitudes for the third star from an isochrone fitting the cluster's CMD and found a value that put the brightest eclipsing star near the isochrone. This assumption might not be correct if tidal interactions with component B result in significant changes to the star's temperature. However, based on the results from other close binaries, we expect stars with less massive surface convection zones (like WOCS 40007 A) to be less affected, as discussed in Section 4.1.

Table 7
Secondary Eclipse Depths for WOCS 40007

Filter	Δm	$N_{\rm ecl}$	$N_{\rm in}$	$N_{\rm out}$
B	0.3850 ± 0.0031	2	4, 3	5, 12
V	0.4013 ± 0.0042	2	12, 2	38, 5
R_C	0.4215 ± 0.0030	3	7, 1, 4	19, 9, 5
I_C	0.4426 ± 0.0071	1	8	26

Note. $N_{\rm ecl}$ is number of observed eclipses, $N_{\rm in}$ is the number of observations made during totality, and $N_{\rm out}$ is the number of out-of-eclipse observations.

4.2.2. WOCS 24009

On the face of it, we might seem to have limited constraints on the distribution of light among the three stars in WOCS 24009. The eclipses of almost equal depth corroborate the idea that the eclipsing stars are nearly identical. However, the precision of the photometry of component A is limited by our ability to disentangle its light from that of the eclipsing binary. Component A's photometry was initially estimated using photometry taken from a theoretical isochrone that fits the cluster CMD, where we assumed that the system was composed of a bright, bluer third star and two fainter, redder stars with identical characteristics. However, realistic solutions for component A and the eclipsing stars cover large ranges (0.9 mag in V for WOCS 24009 A, and 1.5 mag for the eclipsing stars), showing this to be a weak constraint.

We were able to improve the decomposition with information from the BFs (Section 2.3.1) to get a fairly direct measurement of the relative brightness of the three stars in a limited wavelength range within the V passband. This would be an important constraint if the stars only underwent partial eclipses. Closer examination of the light curves indicates that the stars must at least come close to totally eclipsing because the eclipse depths (~0.2 mag) are consistent with the amount of light contributed by the eclipsing stars in the BFs. Indeed, for the best resolved eclipses, there is a brief period of totality, as could occur for stars that differ in radius by less than 4%. The light curve fits also indicate that the inclination of the eclipsing binary is within a degree of being edge-on. This news means that the system photometry can be precisely decomposed: the light from component C in the eclipsing binary is directly measurable from the secondary eclipse depth, the similarity of component B along with light curve fits can then constrain its contribution, and the bright component A is the remainder.

Because the period of totality is so brief and the contribution of component A is so large, it is not as feasible to use a direct measurement of the secondary eclipse depth in the same way as we did for WOCS 40007 above. We therefore derived light ratios from our light curve analysis and used them to decompose the system's photometry. Although we did use the BF light constraints in our models, the final light ratios are driven by the existence of the total eclipse and the near identical characteristics of the eclipsing stars.[16] The

[16] For completeness, we note that the derived value of $l_3 = L_A/(L_A + L_B + L_C) = 0.614$. This underscores that the BF values from Section 2.3.1 were systematically in error as a result of the significant temperature difference between component A and the eclipsing stars. However, the light curve fit overrode the constraint value we used.

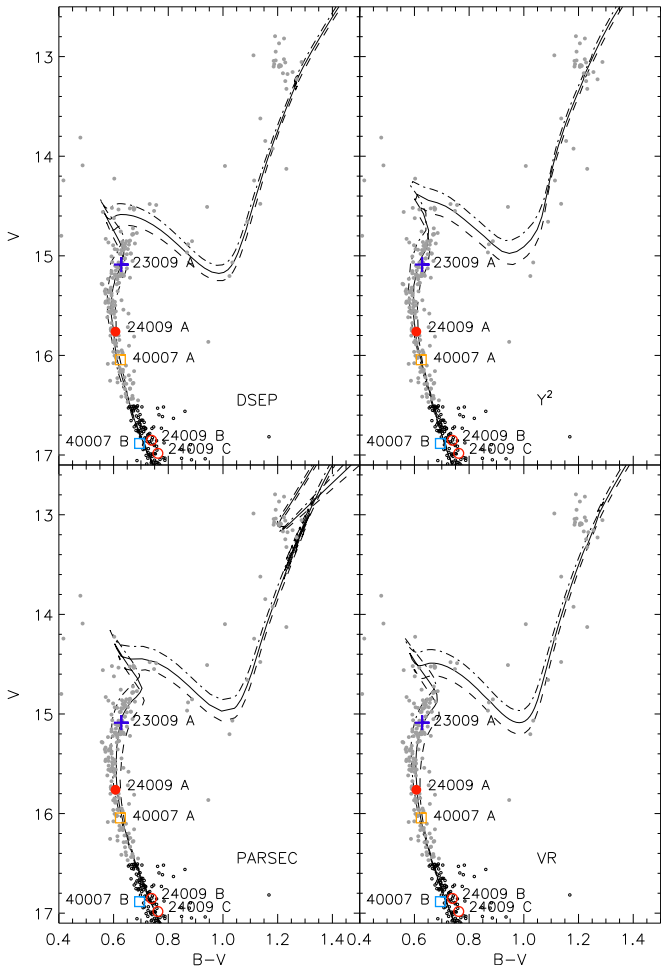

Figure 7. *BV* CMD (Kalirai et al. 2001) for NGC 6819 with removal of nonmembers having $V \leqslant 16.5$. Differential reddening corrections from Platais et al. (2013) are applied to each star. Isochrones are plotted with $Z \approx 0.015$ and ages 2.3, 2.5, and 2.7 Gyr for PARSEC and VR, while DSEP show 2.5, 2.7, 2.9 Gyr and Y^2 use 2.2, 2.4, and 2.6 Gyr; all use $E(B-V) = 0.16$ and $(m-M)_V = 12.40$. The decomposed photometry for WOCS 24009 is shown as the set of red points with the bright third star (filled circle) and the dimmer eclipsing stars (empty circles). WOCS 23009 A (purple +) along with WOCS 40007 A (orange □) and B (blue □) stars are indicated.

decomposed photometry of WOCS 24009 is given in Table 3. The color of the bright A component is consistent with the spectroscopic temperature for our preferred reddening, and all three stars fall within the band of the main sequence in the CMD. The decomposed photometry of WOCS 24009 can be found in Figure 7 along with the other measured cluster members.

Although we can find isochrones that fit the masses and photometry of the eclipsing stars of each binary (WOCS 40007 and WOCS 24009) separately to within 1σ, there are no solutions that simultaneously fit all four stars that precisely. A distance modulus of $(m-M)_V \approx 12.45$ threads through the error ellipses for all of the stars at a little more than 1σ away, but we must consider the possibility of systematic errors. The relative brightnesses of the stars in each binary are consistent with their masses for models with a wide range of ages and compositions. However, the components of WOCS 40007 imply a smaller distance modulus than WOCS 24009 by about 0.1 mag. Differential reddening is a natural place to seek an explanation for this discrepancy because the Platais et al. (2013) map appears to be over-correcting WOCS 40007: both components appear to be bluer than the corrected main sequence, and WOCS 40007 B is significantly brighter than WOCS 24009 C in spite of a smaller measured mass. However, to bring the WOCS 40007 stars back to the cluster main sequence, the reddening correction would need to be well outside of the distribution of corrections for nearby stars (within about an arcmin). Proper-motion and RV information argues against the idea that WOCS 40007 is a foreground nonmember system. Our current best explanation is that the WOCS 40007 star characteristics have been affected by star–star interactions in the case of component B, and by imperfectly determined corrections for the faint third star star in the case of component A.

4.2.3. WOCS 23009

The simplest case is the long period binary WOCS 23009. The small amplitude of the total secondary eclipse in the *Kepler* photometry (0.002 mag; Sandquist et al. 2013a) indicates that we can treat the system photometry as essentially identical to that of the brightest eclipsing star—any corrections would be less than the uncertainty in the system magnitude. In all of the measured DEBs in NGC 6819, WOCS 23009 A is potentially the best indicator of age for the cluster, as it is the most evolved star with a measured radius.

We have updated our estimate of the mass of WOCS 23009 A using the photometry and masses of our eclipsing binary star measurements. Sandquist et al. (2013a) determined the mass of WOCS 23009 A to be $1.468 \pm 0.030\,M_\odot$ using an isochrone-based extrapolation from the masses and photometry of the components of the binary WOCS 40007. It is almost certainly more massive than WOCS 24009 A, but it is part of a single-lined binary and so its mass could only be estimated from its CMD position relative to other cluster stars of known mass. Our preferred fit uses the two WOCS 24009 stars because of larger concerns about the photometry of the WOCS 40007 stars. Fits for a choice of isochrone (from a particular research group with specific composition and age) give uncertainties of about $\pm 0.010\,M_\odot$ for the mass of WOCS 23009 A, with an additional $0.004\,M_\odot$ coming from uncertainty in the V magnitude of WOCS 23009. However, there are larger systematic differences. Using $Z = 0.015$, Dartmouth (DSEP; Dotter et al. 2008) and Victoria-Regina (VR; VandenBerg et al. 2006) isochrones produce similar masses (1.472–$1.476\,M_\odot$), while the PARSEC (Bressan et al. 2012) models give a lower mass ($1.458\,M_\odot$). The lower mass for the PARSEC isochrones may be due to a larger assumed convective core overshooting (approximately 0.25 pressure scale heights H_P versus $0.2H_P$ for other models) or a higher assumed helium abundance ($\Delta Y \approx 0.007$) for a given metal content. When varying the metal content along with the helium content (assuming, like most stellar modelers, that there is a constant $\Delta Y/\Delta Z$), there are smaller systematic changes because of the compensating effects of Y and Z: reducing the metal content from $Z = 0.015$ to $Z = 0.012$ reduces the mass of WOCS 23009 A by about $0.004\,M_\odot$. Based on these considerations, we estimate the systematic uncertainty due to model differences to be $\pm 0.008\,M_\odot$.

Our new estimate of the mass of WOCS 23009 A is $1.464 \pm 0.011 \pm 0.012\,M_\odot$, where the two uncertainties are estimates of the random and systematic effects, and we have taken the central value to be between the PARSEC and DSEP/

VR values using $Z = 0.012$ and 0.015. This is consistent with our original estimate ($1.468 \pm 0.03\,M_{\odot}$, Sandquist et al. 2013a). The main changes in the analysis are the revision in the metal content of the models we use and the different sample of stars used for the mass estimation. If we were to use the stars of WOCS 40007 instead, we would get a mass for WOCS 23009 A that is about $0.02\,M_{\odot}$ lower. We hope that in the future we can reconcile the characteristics of WOCS 40007 with those of the other eclipsing systems, but right now we believe there are still unidentified systematic issues present.

Because the radius of the star is mildly correlated with the mass estimate used (Sandquist et al. 2013a), we have re-run fits to the RVs and eclipse light curves of WOCS 23009. The updated values are shown in Table 3.

4.3. Distance Modulus

When radius and temperature can be determined for eclipsing binary stars, the distance can be derived by comparing the predicted absolute magnitude to photometric observations. We used the photometric temperature estimates from Section 2.3.2 along with the binary star radii to derive luminosities, applied bolometric corrections from VandenBerg & Clem (2003) to compute absolute V magnitudes, and used V magnitudes from Yang et al. (2013) photometry to derive the distance modulus. For four out of the five eclipsing binary stars we discuss here (WOCS 23009 A, WOCS 24009 B and C, and WOCS 40007 A) we get very consistent distance moduli. For the remaining star (WOCS 40007 B), the difference is likely due to problems determining the photometric temperature: $(B - V)$ and $(V - I)$ colors for the star puts it on the blue and red sides of the main sequence, respectively. If we adopt a temperature consistent with those of WOCS 24009 B and C (very close to WOCS 40007 B in the CMD), the distance modulus comes into agreement with those of the other stars.

After propagating uncertainties due to the mean cluster reddening, differential reddening, and the decomposition of the photometry of the binary components, we find typical uncertainties of around 80–100 K in the photometric temperatures. The uncertainty in the temperature dominates the error budget for the distance modulus, which we find to be about 0.08 mag for each star. The individual distance values are given in Table 3. The weighted average is $(m - M)_V = 12.38 \pm 0.04$, where the quoted uncertainty is the error in the mean. This is consistent with the recent value (12.40 ± 0.12) derived by Anthony-Twarog et al. (2014) in a comparison of the CMD with Yonsei-Yale (Y^2; Demarque et al. 2004) isochrones. Our distance modulus determination is less explicitly dependent on the choice of metallicity, although it does enter through the photometric temperature determination. However, a 0.1 dex shift in [Fe/H] only results in a 15 K change in temperature and about a 0.01 mag shift in the distance modulus.

4.4. Age Constraints

When fitting isochrones to cluster CMDs, age information comes from the photometry of stars around the main sequence turnoff. As a baseline comparison (Figure 7), we first employed the conventional method of comparing isochrones to cluster photometry using a reddening and distance modulus, in this case determined by Anthony-Twarog et al. (2014). We used the photometry of Kalirai et al. (2001) due to its high signal-to-noise ratio (and small scatter) for main sequence stars near the turnoff. To minimize the scatter, we also applied the differential reddening correction map used by Platais et al. (2013). We further cleaned the CMD by restricting the sample to single-star cluster members brighter than the $V \sim 16.5$ mag limit from the WOCS RVs survey (Milliman et al. 2014) and to stars with proper-motion membership probabilities greater than 50% from either Platais et al. (2013) or Sanders (1972). The decomposed photometry of WOCS 24009 is plotted along with the photometry of other observed DEB stars: WOCS 23009 A (Sandquist et al. 2013a) and both eclipsing components of WOCS 40007 (Jeffries et al. 2013). The tabulated photometry of the cluster DEB stars can be found in Table 3. To facilitate clean comparisons between isochrone sets as discussed at the beginning of Section 4, we use a common value of $Z \approx 0.015$ for all of the isochrone sets: DSEP, PARSEC, VR, and Y^2. Figure 8 uses V and I_c photometry from Yang et al. (2013) and also applies differential reddening corrections to the CMD. The isochrones do a decent job of fitting the VI_c photometry along the main sequence, turnoff, and subgiant branches except for Y^2 models, which appear to be too blue for the cluster stars as well as PARSEC models to a lesser extent. Due to distance and reddening uncertainty for the cluster, forcing isochrones to fit well-measured stars at their observed V magnitude, color, *and* mass is a more robust way of comparing isochrones to the

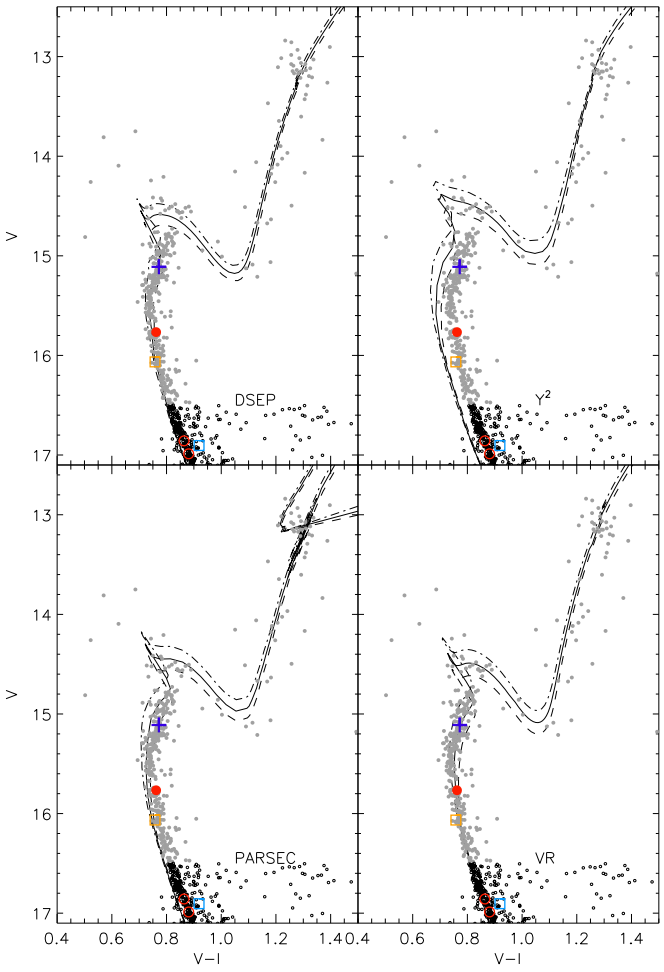

Figure 8. VI_C CMD for NGC 6819 (Yang et al. 2013) with isochrones employing $E(V - I) = 0.20$ and $(m - M)_V = 12.40$. Otherwise the isochrone ages and symbols are the same as Figure 7.

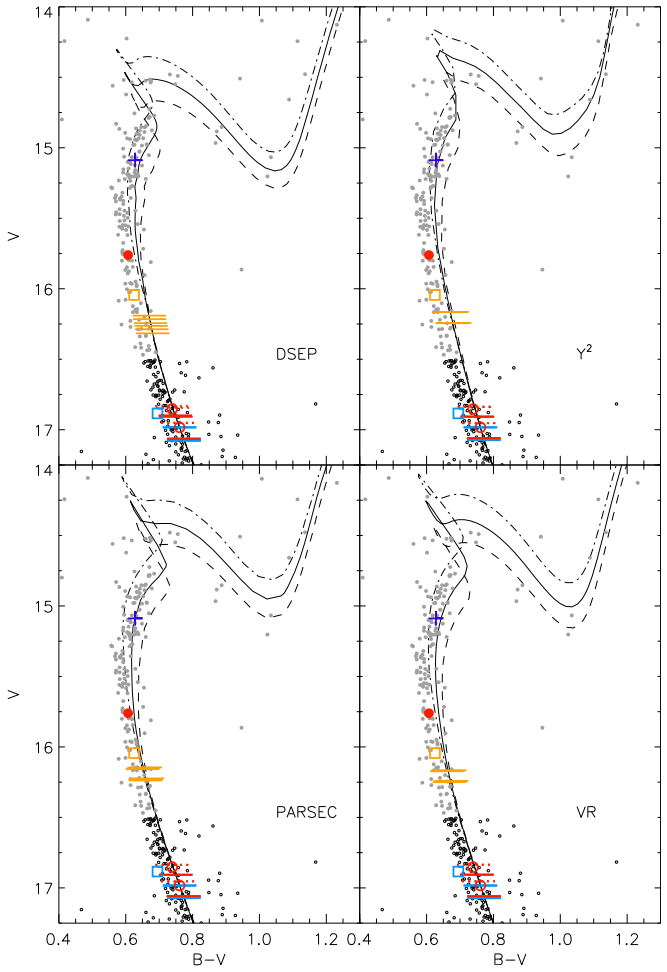

Figure 9. *BV* CMD for NGC 6819 with $Z \approx 0.015$ isochrones shifted to match the photometry of WOCS 24009 C at its measured mass, as discussed in Section 4.4. The symbols for the plotted cluster stars are the same as Figure 7. Horizontal lines delimit the range for the 1σ uncertainty in the mass for components. Those for WOCS 24009 are red dotted lines for component B and solid for component C. Plotted ages are 2.1, 2.3, and 2.5 Gyr for DSEP and PARSEC; 2.0, 2.2, 2.4 for VR and Y^2.

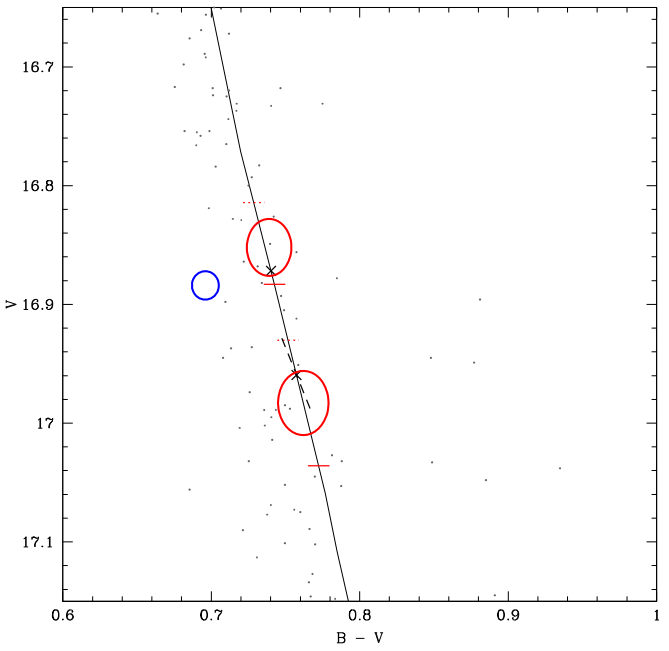

Figure 10. *BV* CMD for NGC 6819 zoomed on the fainter components of WOCS 24009 (red) and WOCS 40007 (blue), shown with a 1σ error ellipses for their photometry. A 2.3 Gyr $Z \approx 0.015$ PARSEC isochrone is plotted with the predicted positions of stars of masses equal to WOCS 24009 B and C (×) and the 1σ mass uncertainties (horizontal lines). The isochrone is shifted to optimize the matches to the photometry of WOCS 24009 B and C at their measured masses. The effects of a ± 0.01 mag uncertainty in the differential reddening color correction is shown with the black dashed line.

CMD. We chose to align the models with WOCS 24009 C in Figure 9 because of its precise decomposed photometry, and by doing so there is no need to assume a reddening and distance modulus. This type of differential comparison, where we shift all isochrones to match mostly unevolved main sequence stars, uses the isochrone shape at the turnoff and brightness as the age indicator. In the comparison here, the isochrones do a satisfactory, if imperfect, job of matching the characteristics of the fainter eclipsing stars. For example, isochrones predict that a star with the measured mass of WOCS 40007 A should be fainter relative to the three stars with mass in the range $1.005 < M/M_{\odot} < 1.010$—compare the inferred position of the star with the range predicted based on its measured mass (delimited by horizontal lines). However, there are lingering uncertainties in the photometric decomposition of WOCS 40007 A due to the faint third star (described in Section 2.3.1) that may alleviate this issue. Future refinements of the mass of WOCS 24009 A should help identify whether this is a serious issue with the models.

The most age sensitive features of the CMD at present are the photometric positions of WOCS 23009 A and the stars on the turnoff and subgiant branch. WOCS 23009 A is valuable because its companion is rather faint, so that we can be assured that its measurements accurately represent the photometry of a single star. Unfortunately, we cannot directly measure its mass. In addition, there are uncertainties in the fit due to uncertainty in the mass and photometric decomposition of WOCS 24009 C, and in the relative differential reddening corrections for WOCS 23009 A and 24009 C. All of these affect where the isochrones should be pinned at the faint end. The mass uncertainty is the dominant uncertainty (see Figure 10), leading to an uncertainty of about ± 0.08 mag in the isochrone placement. The fit to the combination of WOCS 24009 B and C can be improved by a brightward shift of 0.02 to the isochrones—both components can be matched to within the uncertainties on the masses and decomposed photometry, as shown in Figure 10. Regardless of that choice, these uncertainties together lead to an uncertainty of about 0.1 Gyr in the age implied by WOCS 23009 A. Based on the comparison with $Z \approx 0.015$ models, the implied ages are 2.12 Gyr for VR, 2.15 Gyr for Y^2, 2.21 Gyr for DSEP, and 2.31 Gyr for PARSEC. Based on the scatter in these values, we estimate a systematic uncertainty of about 0.09 Gyr due to differences in the physics encoded in the models.

The turnoff and subgiant stars are more numerous and contain age information, but we have imperfect knowledge of whether they might be in undetected multiple star systems. At the turnoff (the bluest point on the isochone) and fainter, the blue side of the observed distribution of main sequence stars can usually be expected to be a good representation of the single star main sequence because unresolved binaries would be displaced brighter and redder. Brighter than the turnoff, however, unresolved binaries can fall either redder or bluer than the single star sequence. On the subgiant branch, binarity

can affect the color in either direction, but the lower envelope of the subgiant stars can trace out the single star sequence. Using proper-motion and RV information from Milliman et al. (2014), we plotted the most likely single star subgiant cluster members on all of our CMDs: WOCS 7008, 8004, 9009, 11005, 11006, 18002, 20016, 22004, 22013, and 23006. Satisfactory fits are possible with each of the isochrone sets, but the color of the turnoff and the brightness of the faint envelope of the subgiant branch appear to be poorly matched. Part of this may be uncertainties in the measured positions of the faint eclipsing stars we use to pin the isochrones, but the shapes of the isochrones on the subgiant branch and at the top of the main sequence can be importantly affected by the modeling of convective core overshooting. For example, the DSEP models appear to do the best job of simultaneously matching the properties of WOCS 23009 A and the fainter subgiant branch stars. Without additional work on the subgiants and their modeling, it is too early to weight them in the determination of the age presented here.

Uncertainties in metallicity also produce a potential source of systematic error though. We examined isochrone fits using a decreased metal abundance $Z = 0.012$ in Figure 11. When using a lower metal abundance, the isochrones used to best fit the cluster are younger by about 0.1 Gyr compared to isochrones using $Z = 0.015$. The main sequence shape seems to be somewhat more poorly fit for all four isochrone sets. From all of the considerations of the CMD, we quote an age of $2.21 \pm 0.10 \pm 0.20$ Gyr, where the quoted uncertainties are from the combined fitting uncertainties and the combined systematic uncertainties. The shifts needed to match the photometry of WOCS 24009 C at its measured mass imply particular values of reddening and distance modulus, and for completeness, we give them here. For the four sets of isochrones we have discussed, we find reddenings $0.23 < E(B-V) < 0.26$ and distance moduli $12.56 < (m-M)_V < 12.67$ for $Z = 0.012$, and $0.19 < E(B-V) < 0.22$ and $12.46 < (m-M)_V < 12.57$ for $Z = 0.015$. These values are affected by differences in input physics and color–temperature relations used for the different isochrone sets, and we do not consider them to be measurements of these values.

The most direct method of comparing eclipsing binary observations to theory is through the M–R plane. The radii of evolved stars are good age indicators because the physical measurements in an eclipsing binary system can reach a high degree of precision while avoiding sources of systematic error from sources such as distance and reddening. Statistically speaking, it is best to use all well-measured stars for determining the cluster age, and with the analysis of WOCS 24009, we add two more stars. (Unfortunately, WOCS 24009 A does not undergo eclipses, and so its radius cannot be measured directly and it cannot be used in this analysis.) The masses and radii for WOCS 24009 and the other cluster stars used in determining age are listed in Table 3. Note that the values for WOCS 40007 A and B have been updated for this paper after improved corrections for the effects of the faint third star on RVs and eclipse timings, and the incorporation of *Kepler* photometry. Figure 12 shows the M–R diagram comparison with isochrones assuming the higher metal abundance $Z = 0.015$. For all model sets using the higher metal content, the eclipsing stars of WOCS 40007 lie slightly above the isochrone that best matches the bright star WOCS

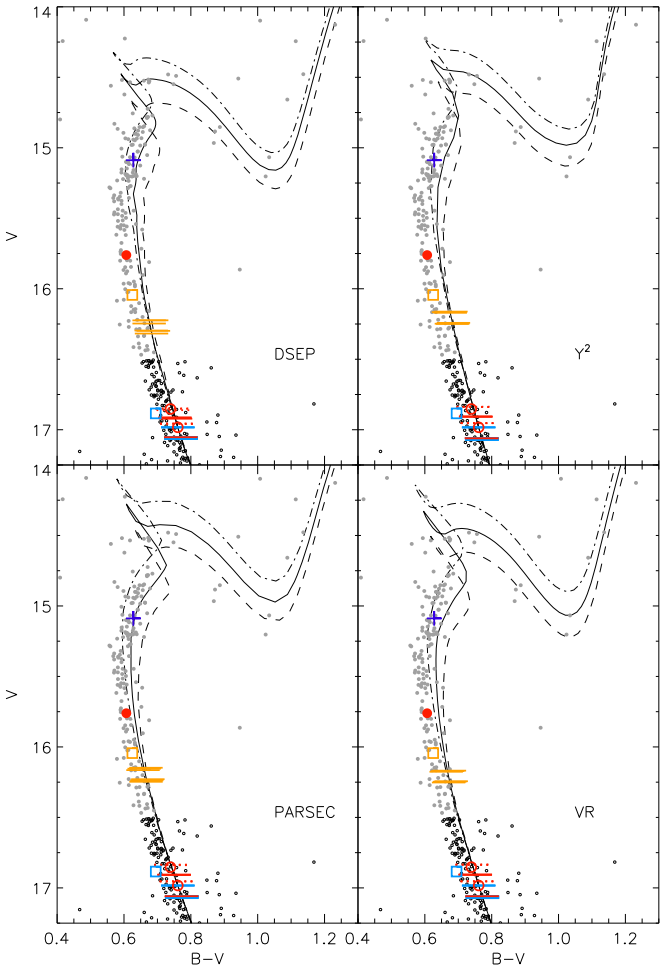

Figure 11. *BV* CMD (Kalirai et al. 2001) for NGC 6819 with $Z \approx 0.012$. All isochrones are shifted in the same way as in Figure 9, and symbols are the same. Plotted isochrone ages are 2.0, 2.2, and 2.4 Gyr for DSEP, PARSEC, VR, and Y^2.

23009 A and the eclipsing stars 24009 B and C. Based on the Anthony-Twarog et al. (2014) suggestion of a lower metallicity, we examined a metal abundance $Z = 0.012$ (decreased by about 0.1 dex and consistent with plausible errors in the metallicity scale) as seen in Figure 13. With a lower metallicity the eclipsing stars fall on younger models, similar to what is seen in the CMDs with the same Z content. The model radii decrease and produce a small improvement to the consistency of the ages implied by the different stars and a small (∼0.2 Gyr) reduction to the age.

The most age-sensitive eclipsing star currently known in the cluster is WOCS 23009 A, and the age uncertainty derived from this star alone is mostly responsible for the error in the weighted mean. It should be remembered that its mass comes from an isochrone-based extrapolation from the properties of WOCS 24009 stars as mentioned in Section 4.2, but that the radius is not terribly sensitive to this estimate (see Sandquist et al. 2013a for a discussion) and this is why this star can provide age discrimination. With the improved RV measurements presented here, the mass uncertainties for the stars in WOCS 40007 and WOCS 24009 have been reduced compared to what was presented in Jeffries et al. (2013). The eclipsing stars for those two systems appear to imply slightly different ages, although this is not at a high level of significance. For

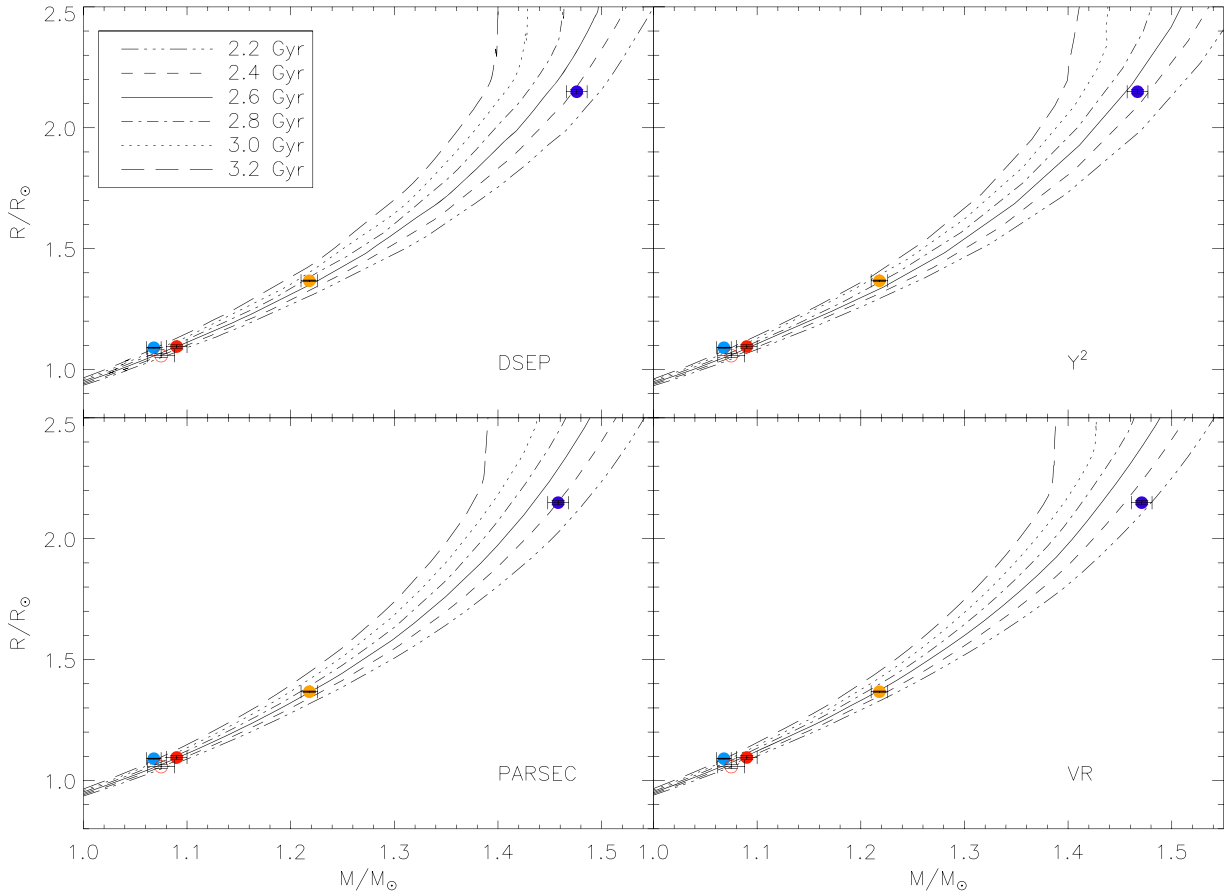

Figure 12. Mass–radius (*M–R*) plot for WOCS 24009 B and C (red filled and empty circles), WOCS 40007 A (orange) and B (blue), and WOCS 23009 A (purple) as the most massive component. The plotted isochrones employ $Z = 0.015$ and $[\alpha/\mathrm{Fe}] = 0.0$. The masses used for WOCS 23009 A are derived from extrapolations using the plotted isochrone set.

example, the three faintest stars (WOCS 40007 B and WOCS 24009 B and C) have masses that are consistent with each other at a little under a 2σ level. As discussed in Section 4.1, WOCS 40007 B may have been inflated in radius due to tidal interaction, and its V-band photometry may also have been affected, making its use in the CMD age determination questionable. Depending on the isochrones used, the remaining three stars are roughly consistent with the age derived from WOCS 23009 A at about the 1σ level.

The error in the weighted average is about 0.05 Gyr, but the systematic sources of error are more substantial. A major systematic contribution is uncertainty in the metal content of the stars. We find differences of 0.13–0.20 Gyr between models having $Z = 0.012$ and $Z = 0.015$ from the same research group, with the lower metallicity producing lower ages. As a result, we estimate the systematic metallicity uncertainty to contribute an uncertainty of ± 0.10 Gyr to the age. Comparing results from different research groups for the same *Z*, there is a 0.2–0.25 Gyr range, with VR models giving the lowest ages (2.22 Gyr for $Z = 0.0125$), Y^2 models giving the highest (2.40 Gyr for $Z = 0.012$), and DSEP and PARSEC models returning values nearly midway between these values. Based on this, we estimate a systematic uncertainty of about ± 0.12 Gyr on the age due to differences in physics and chemical mixes used in the different models.

Because we do not have strong reason to prefer one metal content *Z* or one set of models, we take our best *M–R* estimate of the age to be in the middle of the ranges and quote an age of $2.38 \pm 0.05 \pm 0.22$ Gyr, where the two uncertainties are statistical and systematic, respectively. Although we can expect an improvement of the statistical uncertainty in the age with additional measurement of the eclipsing stars, the best way of improving the age estimate in the cluster will be to reduce the metallicity uncertainty (through a combination of improved spectroscopic measurements of cluster star abundances relative to the Sun and a resolution of the question of the solar value $Z_\odot$) and the model isochrone uncertainties.

5. CONCLUSIONS

We have presented extensive photometric and spectroscopic observations of the detached eclipsing binary WOCS 24009 in open cluster NGC 6819 as part of a larger effort to obtain the age of the cluster using all of the useful binaries (including WOCS 40007 and WOCS 23009). Our modeling indicates that we have obtained mass and radius measurements with uncertainties ~1.0% and 0.5% for the eclipsing components of WOCS 24009. We have started to characterize the turnoff-mass WOCS 24009 A, although the uncertainty in its mass is about 4.6%. This uncertainty can be reduced with a combination of RV measurements of component A and eclipse timings—together these measurements will provide the highest precision measurement of the third star's orbit and the mass ratio $q_A = M_A/(M_B + M_C)$. Because the star's photometry can be disentangled from the eclipsing stars, a more precise mass will provide a significantly better constraint on the cluster age.

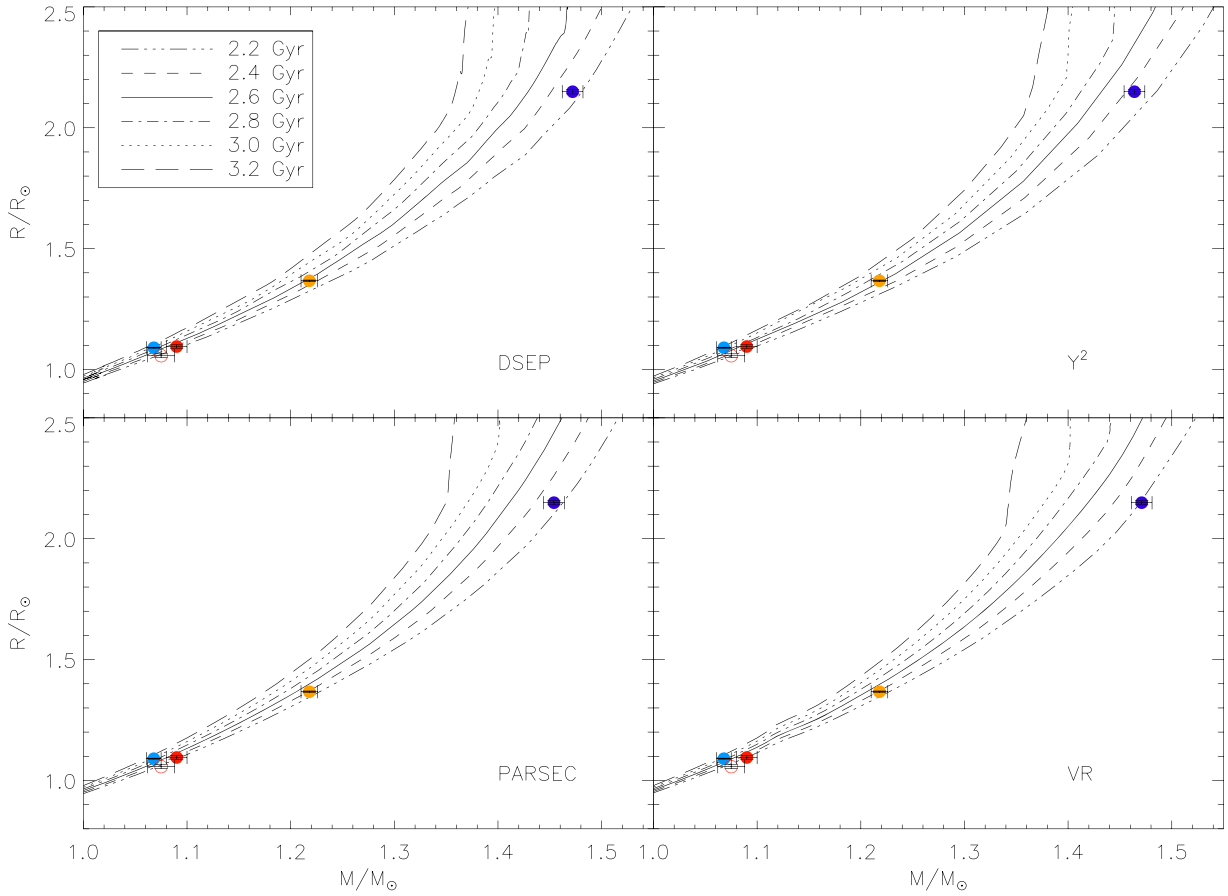

Figure 13. *M–R* plot for isochrones with a lower metal abundance $Z = 0.012$. Star symbols are the same as in Figure 12.

Systematic uncertainties in the theoretical stellar models and in the metal content of the cluster stars are the main obstacles to a higher precision age at present. We derive ages for NGC 6819 of $2.21 \pm 0.10 \pm 0.20$ Gyr using the CMD and $2.38 \pm 0.05 \pm 0.22$ using the *M–R* plane, where the quotes are estimates of statistical and known systematic uncertainties. There is still significant disagreement between different indicators of the cluster metallicity, and a better determination of this would significantly reduce the systematic errors quote above. The possibility of a lower cluster metallicity can be spectroscopically tested in the future using the binary stars with the assistance of constraints on the surface gravities from the binary star analysis. Our derived age is in agreement with asteroseismic (Basu et al. 2011) and white dwarf cooling (Bedin et al. 2015) ages for the cluster.

Stellar model differences remain one of the biggest contributors to the uncertainty in the age. To reduce this source of error, it is helpful to review the systematic differences between model sets even if we cannot be completely certain of the causes. In the *M–R* comparisons made at the same metal content *Z*, VR isochrones gave the youngest ages of the model sets we tested, and Y^2 returned the largest ages. In CMD comparisons, VR, Y^2, and DSEP models gave similar ages, with PARSEC models returning the oldest age. The dependencies of these comparisons on different model inputs (chemical composition mix, the treatment of core convection and diffusion, and color–temperature transformations, among others) should continue to help drive us toward more accurate models.

We would like to thank the former Director of Mount Laguna Observatory (P. Etzel) for generous allocations of observing time; A. Talamantes, E. Bavarsad, and D. Baer for assistance with data taking at MLO; and D. Short for his calculations testing the three-body orbital dynamics of this system.

This paper includes data collected by the *Kepler* mission. Funding for the *Kepler* mission is provided by the NASA Science Mission directorate. We are grateful to the *Kepler* team for the opportunity to work with such an extensive and precise dataset. We gratefully acknowledge funding from the National Science Foundation under grant AST-0908536 to San Diego State University and AST-0908082 to the University of Wisconsin-Madison, and from the National Aeronautics and Space Administration (NASA) under grant G00008957. KB acknowledges funding from the Carlsberg Foundation and the Willum Foundation. Funding for the Stellar Astrophysics Centre is provided by The Danish National Research Foundation (grant agreement No. DNRF106). The research is supported by the ASTERISK project (ASTERoseismic Investigations with SONG and *Kepler*) funded by the European Research Council (grant agreement No. 267864). AMG is funded by a National Science Foundation Astronomy and Astrophysics Postdoctoral Fellowship under Award No. AST-1302765.

REFERENCES

Andersen, J. 1991, A&ARv, 3, 91
Anthony-Twarog, B. J., Deliyannis, C. P., & Twarog, B. A. 2014, AJ, 148, 51

Asplund, M., Grevesse, N., & Sauval, A. J. 2005, in ASP Conf. Ser. 336, Cosmic Abundances as Records of Stellar Evolution and Nucleosynthesis, ed. T. G. Barnes III, & F. N. Bash (San Francisco, CA: ASP), 25
Asplund, M., Grevesse, N., Sauval, A. J., & Scott, P. 2009, ARA&A, 47, 481
Auner, G. 1974, A&AS, 13, 143
Avni, Y. 1976, ApJ, 210, 642
Basu, S., Grundahl, F., Stello, D., et al. 2011, ApJL, 729, L10
Batalha, N., Borucki, W., Koch, D. G., et al. 2010, ApJL, 713, L109
Bedin, L. R., Salaris, M., Anderson, J., et al. 2015, MNRAS, 448, 1779
Borucki, W., Koch, D. G., Basri, G., et al. 2010, Sci, 327, 977
Bragaglia, A., Carretta, E., Gratton, R. G., et al. 2001, AJ, 121, 327
Bressan, A., Marigo, P., Girardi, L., et al. 2012, MNRAS, 427, 127
Brogaard, K., Bruntt, H., Grundahl, F., et al. 2011, A&A, 525, A2
Brogaard, K., VandenBerg, D. A., Bruntt, H., et al. 2012, A&A, 543, A106
Burkhead, M. S. 1971, AJ, 76, 251
Caffau, E., Ludwig, H.-G., Steffen, M., Freytag, B., & Bonifacio, P. 2011, SoPh, 268, 255
Caldwell, D. A., Kolodziejczak, J., Van Cleve, J., et al. 2010, ApJL, 713, L92
Casagrande, L., Ramírez, I., Meléndez, J., Bessell, M., & Asplund, M. 2010, A&A, 512, AA54
Chabrier, G., Gallardo, J., & Baraffe, I. 2007, A&A, 472, L17
Claret, A. 2000, A&A, 363, 1081
Clausen, J. V., Bruntt, H., Claret, A., et al. 2009, A&A, 502, 253
Clausen, J. V., Bruntt, H., Olsen, E. H., Helt, B. E., & Claret, A. 2010, A&A, 511, A22
Coelho, P., Barbuy, B., Meléndez, J., Schiavon, R. P., & Castilho, B. V. 2005, A&A, 443, 735
Demarque, P., Woo, J.-H., Kim, Y.-C., & Yi, S. K. 2004, ApJS, 155, 667
Dotter, A., Caboyer, B., Jevremovic, D., et al. 2008, ApJS, 178, 89
Geller, A. G., Mathieu, R. D., Harris, H. C., & McClure, R. D. 2008, AJ, 135, 2264
Gililand, R., Jenkens, J., Borucki, W., et al. 2010, ApJL, 713, L160
González, J. F., & Levato, H. 2006, A&A, 448, 283
Hauschildt, P. H., Baron, E., & Allard, F. 1997, ApJ, 483, 390
Hinkle, K., Wallace, L., Harmer, D., Ayres, T., & Valenti, J. 2000, in IAU Meeting 24, Joint Discussion 1, Atomic and Molecular Data for Astrophysics: New Developments, Case Studies, and Future Needs, 26
Hole, K. T., Geller, A. M., Mathieu, R. D., et al. 2009, AJ, 138, 159
Honeycutt, R. K. 1992, PASP, 104, 435
Jeffries, M. W., Jr., Sandquist, E. L., Mathieu, R. D., et al. 2013, AJ, 146, 58
Kalirai, J. S., Richer, H. B., Fahlman, G. G., et al. 2001, AJ, 122, 266
Kaluzny, J., & Shara, M. M. 1988, AJ, 95, 785
Koch, D. G., Borucki, W., Basri, G., et al. 2010, ApJL, 713, L79
Lee-Brown, D. B., Anthony-Twarog, B. J., Deliyannis, C. P., Rich, E., & Twarog, B. A. 2015, AJ, 149, 121
Lindoff, U. 1972, A&AS, 7, 497
Mathieu, R. D. 2000, in ASP, 198, 517
Meibom, S., Barnes, S. A., Latham, D. W., et al. 2011, ApJL, 733, L9
Meibom, S., Barnes, S. A., Platais, I., et al. 2015, Natur, 517, 589
Mészáros, S., Holtzman, J., García Pérez, A. E., et al. 2013, AJ, 146, 133
Milliman, K. E., Mathieu, R. D., Geller, A. M., et al. 2014, AJ, 148, 38
Orosz, J. A., & Hauschildt, P. H. 2000, A&A, 364, 265
Platais, I., Gosnell, N. M., Meibom, S., et al. 2013, AJ, 146, 43
Popper, D. M., Lacy, C. H., Frueh, M. L., & Turner, A. E. 1986, AJ, 91, 383
Rosvick, J. M., & Vandenberg, D. A. 1998, AJ, 115, 1516
Rucinski, S. M. 1992, AJ, 104, 1968
Rucinski, S. M. 2002, AJ, 124, 1746
Sanders, W. L. 1972, A&A, 19, 155
Sandquist, E. L., Latham, D. W., Shetrone, M. D., & Milone, A. A. E. 2003, AJ, 125, 810
Sandquist, E. L., Mathieu, R. D., Brogaard, K., et al. 2013a, ApJ, 762, 58
Sandquist, E. L., Shetrone, M., Serio, A. W., & Orosz, J. 2013b, AJ, 146, 40
Stello, D., Meibom, S., Gilliland, R. L., et al. 2011, ApJ, 739, 13
Stetson, P. B. 1987, PASP, 99, 191
Street, R. A., Horne, K., Lister, T., et al. 2002, MNRAS, 330, 737
Street, R. A., Horne, K., Lister, T., et al. 2003, MNRAS, 340, 1287
Street, R. A., Horne, K., Lister, T., et al. 2005, MNRAS, 358, 795
Talamantes, A., Sandquist, E. L., Clem, J. L., et al. 2010, AJ, 140, 1268
Tegmark, M., Strauss, M. A., Blanton, M. R., et al. 2004, PhRvD, 69, 103501
Torres, G., Andersen, J., & Giménez, A. 2010, A&ARv, 18, 67
Torres, G., Lacy, C. H., Marschall, L. A., Sheets, H. A., & Mader, J. A. 2006, ApJ, 640, 1018
VandenBerg, D. A., Bergbusch, P. A., & Dowler, P. D. 2006, ApJS, 162, 375
VandenBerg, D. A., & Clem, J. L. 2003, AJ, 126, 778
Vos, J., Clausen, J. V., Jørgensen, U. G., et al. 2012, A&A, 540, A64
Yang, S.-C., Sarajedini, A., Deliyannis, C. P., et al. 2013, ApJ, 762, 3